HHS Public Access

Author manuscript

Nat Cell Biol. Author manuscript; available in PMC 2021 August 01.

Published in final edited form as:

Nat Cell Biol. 2021 February ; 23(2): 198–208. doi:10.1038/s41556-020-00625-2.

Optogenetic manipulation of cellular communication using engineered myosin motors

Zijian Zhang[1,2,3], **Nicolas Denans**[2,3,4], **Yingfei Liu**[5,6,7], **Olena Zhulyn**[2,3], **Hannah D. Rosenblatt**[2,3], **Marius Wernig**[5,6], **Maria Barna**[2,3,*]

[1]Department of Chemical and Systems Biology, Stanford University, Stanford, California 94305, USA.

[2]Department of Developmental Biology, Stanford University, Stanford, California 94305, USA.

[3]Department of Genetics, Stanford University, Stanford, California 94305, USA.

[4]Present address: Stowers Institute for Medical Research, Kansas City, MO 64110, USA.

[5]Institute for Stem Cell Biology and Regenerative Medicine, Stanford University, Stanford, California 94305, USA.

[6]Department of Pathology, Stanford University, Stanford, California 94305, USA.

[7]Present address: Institute of Neurobiology, Xi'an Jiaotong University Health Science Center, Xi'an, Shaanxi 710061, China.

Abstract

Cells achieve highly efficient and accurate communication through cellular projections such as neurites and filopodia, yet there is a lack of genetically encoded tools that can selectively manipulate their composition and dynamics. Here, we present a versatile optogenetic toolbox of artificial multi-headed myosin motors that can move bidirectionally within long cellular extensions and allow for the selective transport of GFP-tagged cargo with light. Utilizing these engineered motors, we could transport bulky transmembrane receptors and organelles as well as actin remodelers to control the dynamics of both filopodia and neurites. Using an optimized *in vivo* imaging scheme, we further demonstrate that upon limb amputation in axolotls, a complex array of filopodial extensions is formed. We selectively modulated these filopodial extensions and showed that they re-establish a Sonic Hedgehog signaling gradient during regeneration. Considering the ubiquitous existence of actin-based extensions, this toolbox shows the potential to manipulate cellular communication with unprecedented accuracy.

* mbarna@stanford.edu.

Author contributions

Z.Z., N.D. and M.B. conceived the project. N.D., Z.Z. and M.B. designed and constructed the expression vectors. Z.Z. and M.B. planned the experiments. Z.Z. and N.D. executed and analyzed the experiments. Y.L., O.Z., H.D.R., M.W. and M.B. contributed to essential cell cultures, reagents and expertise. Z.Z. and M.B. wrote the paper with input from all authors. M.B. supervised all aspects of the work.

Competing interests

The authors declare no competing financial interests.

Introduction

Cells grow long cellular extensions to achieve controlled and precise cellular communication at a distance. Akin to neurons, wherein slender membranous projections enable long-distance cell communication, cellular extensions are capable of both sensing and responding to the environment[1]. Prominent examples include specialized filopodia that traffic signaling proteins over long ranges during tissue development[2,3], fine finger-like macrophage protrusion that are thought to be involved in pathogen clearance[4], and invadopodia that integrate signals from the tumor microenvironment to facilitate tumor cell dissemination[5]. Current methods to manipulate cellular extensions are largely restricted to the genetic knockout of actin regulators or administration of drugs that interfere with the actin cytoskeleton[6,7,8]. Neither approach is capable of specifically altering the composition, dynamics, or cargo that are delivered into these cellular extensions. Therefore, a genetically encoded tool that selectively manipulate cellular protrusions with high spatiotemporal precision is currently critically lacking. Such a tool, if present, would allow for manipulation of a wide variety of cellular extensions such as filopodia, cytonemes, invadopodia, nanotubes, as well as additional specialized cellular appendages including dendrites and axons[2–5,9,10] to address outstanding biological questions in development, disease, and neuroscience.

One common feature of these cellular protrusions is their conserved backbone that primarily consists of unidirectional actin bundles[11,12]. Hence, it may be feasible to manipulate cargo transport within these protrusions if we could artificially manipulate the movement of motor proteins on these actin bundles. However, natural dimeric myosin motors that are responsible for actin-based motility in cells are not ideal candidates due to either low velocity or low processivity, defined as the ability to take many steps along a track before dissociating[13,14]. Recently, the performance of myosin motors has been extended beyond native characteristics by the creation of four-headed motors that are bound together by flexible spacer elements, which significantly enhanced the velocity and processivity of these artificial motors *in vitro*[15]. However, the ability of such engineered motors to walk along actin filaments within live cells has not been previously examined. Here, we further engineered a suite of such artificial motors that we term “Artificial Transport Vehicles” (ATVs), which are fast, highly processive, optogenetically controlled, and suitable for selectively transporting any GFP-tagged protein at long ranges. We tested ATVs in various contexts including neurons and live organisms. Notably, we were able to directly manipulate the outgrowth of filopodial extensions *in vivo*, leading to the finding of an unexpected role of filopodial extensions in the context of cell signaling and tissue regeneration.

Results

Design and characterization of ATVs

ATVs are modularly designed. The monomeric ATV consists of a myosin head domain, a flexible lever arm domain and a tetramerization domain, which constitutively induces the formation of the active tetrameric form (Fig. 1a, b). Specifically, either myosin XI (plus-ended) or myosin VI (minus-ended) motor heads were truncated and fused to artificial lever arms comprising spectrin repeats, and the fusion of the engineered coiled coil GCN4-pLI

flanked by flexible linkers was used to force tetramerization[15,16]. We further grafted GFP Binding Protein (GBP), a genetically encoded nanobody with a strong affinity towards GFP onto the motors[17], thereby allowing us to anchor any GFP-tagged cargo onto the motor. Importantly, the use of GBP-GFP interaction, instead of direct covalent linkage, in our design, is intended to minimize the effect of motor movement on the normal function of the GFP-tagged cargo. Myosin XI-based plus-ended ATV (ATV+) allows the transport of cargo into cellular extensions, while myosin VI-based minus-ended ATV (ATV−) depletes cargo from the extensions. Since a vast repertoire of fluorescent protein-tagged protein libraries are readily available[18,19], ATVs are designed to be off-the-shelf tools that can be directly applied to any protein that has a florescent protein tag without tailored modifications.

Although these engineered motors hold great potential, their ability to carry out fast and processive unidirectional transport has yet to be confirmed in live cells. Therefore, we first expressed ATVs in the mouse C3H/10T½ embryonic mesenchymal cell line which is known to grow endogenous filopodia[20]. The plus-ended motors accumulated as bright puncta at the tips of filopodia, while the minus-ended motors were centered in the cell body with no observable presence in filopodia (Fig. 1c, Extended Data Fig. 1a-c). We then characterized the velocity of the ATV+ motors with total internal reflection fluorescence (TIRF) microscopy. Long processive runs could be observed and the velocity within filopodia matched well with the *in vitro* measurements at ATP concentration of 0.5 mM, and were measured an order of magnitude faster than most endogenous myosin motors in mammalian cells[15,21] (2.44 ± 0.13 μm/s for ATV+, Extended Data Fig. 1d and Supplementary Video 1).

ATVs transport various cargo proteins to manipulate cellular extensions

We next asked whether we could traffic cargo within extensions using these motors. For example, filopodial extensions appear to traffic key signaling proteins, including components of the Sonic Hedgehog (Shh) pathway, which is utilized in almost every tissue during embryonic development and wherein mutations are found in cancers [2,22,23]. One important cargo to test transport with our ATV motors is the SHH receptor Patched1 (Ptch1), which is a bulky twelve-transmembrane protein that plays a pivotal role in negatively regulating the activity of the Shh pathway and therefore has a critical role in embryogenesis and in tumor suppression[24, 25]. Importantly, Ptch1 is normally localized in primary cilia but has never been observed in filopodia[24], hence we next tested whether artificially transporting Ptch1 within filopodia could be achieved with ATVs. We started by expressing an enhanced GFP (eGFP)-tagged stabilized form of Ptch1 (mouse Ptch1 truncated after the twelfth transmembrane domain to avoid ubiquitin-mediated degradation[26], denoted as sPtch1) with ATV+ in cell culture. Unlike the control without ATV+ expression, sPtch1-eGFP significantly colocalized with ATV+ and accumulated as bright puncta at tips of filopodia (Extended Data Fig. 2a, b). Similar to Ptch1, Dispatched1 (Disp1) is a bulky transmembrane receptor that plays an important role in SHH secretion and long-range cell signaling[27]. Contrary to sPtch1, Disp1 showed intermittent localization along filopodia extensions when overexpressed in cells while the co-expression of Disp1-eGFP with ATV− almost completely depleted Disp1-eGFP from filopodia (Extended Data Fig. 2c, d). Considering that Ptch1 and Disp1 are among the bulkiest proteins with complex structures, these findings

show the potential of ATVs to transport a wide variety of GFP-tagged proteins, including transmembrane proteins.

We next examined whether the ability of ATVs to transport cargo could be utilized to alter the morphology of cellular extensions. Espin1 is an actin-bundling protein that has been reported to create stereocilia when transported by endogenous myosin motors[28]. By co-expressing ATV+ with super folder GFP (sfGFP)-tagged Espin1 in Cos7 cells, which naturally do not grow filopodia, numerous morphologically distinct cellular extensions could be induced *de novo* (length: 12.2 ± 0.3 μm, density: 164.8 ± 7.2 mm^{-1}), while expression of ATV+ or Espin1 alone did not (Fig. 1d-f). We further incorporated our construct into a doxycycline-inducible system to extend our capability to control the outgrowth of filopodia by chemical stimulation. The stable Cos7 cell line expressing this system was found to efficiently generate filopodia after 24 hours of doxycycline treatment (Extended Data Fig. 3). We then tested whether filopodia could be retracted. Myosin X has been reported to be critical for filopodia generation, and the tail domain is responsible for the interaction with specific cargo molecules that are essential for actin-bundling activities[29,30]. Hence, we sought to use ATV− to trap the eGFP-tagged Myosin X tail domain (MyoXtail) within the cell body to generate a functional dominant negative Myosin X[29]. Indeed, the expression of this construct in C3H/10T½ cells could efficiently eliminate filopodia by ~10 fold (from 73.9 ± 6.4 mm^{-1} to 7.6 ± 1.8 mm^{-1}), while the expression of ATV− or MyoXtail alone could not (Fig. 1g-i). In addition, we sought to explore whether artificial filopodia, generated by the expression of a constitutively active mutant of mammalian Diaphanous 2 (mDia2M/A)[31], an F-actin polymerase, could also be eliminated by our ATV motors. We found that ATV− prevented the growth of these artificial mDia2M/A-induced filopodia by actively transporting mDia2M/A-sfGFP back to the cell body in Cos7 cells (Extended Data Fig. 4). Importantly, while GBP-GFP binding preserves the functionality of the cargo, covalently linking the cargo with the motor completely disrupted the cargo function although the cargo was efficiently transported (Extended Data Fig. 5). This result suggests that the steric hindrance of the motor movement may be detrimental to normal cargo function and highlights the importance of using GBP-GFP binding.

Optogenetic ATVs can be activated reversibly with fast kinetics to transport bulky transmembrane receptors

We next decided to further exploit the strong dependence of motor processivity on the oligomeric state of ATVs to create optogenetic counterparts. Cry2olig is a mutant of the cryptochrome 2 from *Arabidopsis thaliana*, and has a desirable light-inducible homo-oligomerization property[32,33]. We swapped the tetramerizing coiled coil domain in the ATVs with Cry2olig to create optoATV+ and optoATV− respectively (Fig. 2a, b). We reasoned that optoATVs would stay monomeric and immobile in the dark, and light stimulation would trigger optoATV oligomerization and initiate the light-induced transport of motors. We first expressed optoATV+ in C3H/10T½ cells and applied a short pulse of blue light to individual cells. Significant accumulation of optoATV+ could be observed at tips of filopodia within 30 seconds (Fig. 2c). Importantly, this process was reversible (activation half-time: ~85s, deactivation half-time: ~210s) and could be repeatedly activated with short pulses of blue light, though with a slight run-down in the activation level (Fig. 2d, Supplementary video 2).

On the other hand, optoATV− could be significantly depleted from filopodia within 2 minutes after blue light stimulation (Fig. 2e, f), but was not noticeably reversible in 10 minutes possibly due to the slow kinetics of optoATV− re-entering filopodia in live cells. With optical control, we were able to measure the velocity of the processive runs of optoATV− within filopodia, which also matched well with *in vitro* results[15] (52.5 ± 2.8 nm/s, Extended Data Fig. 1e) and was measured approximately 3 times the velocity of retrograde flow in fibroblasts[34]. To test the cargo transport capacity, we co-expressed optoATV+ with sPtch1-eGFP in C3H/10T½ cells. A high level of transport and accumulation of sPtch1-eGFP in filopodia could be observed after short pulses of blue light (Fig. 3a, d, Supplementary video 3), and this activation could be efficiently confined to single filopodia using localized illumination (Fig. 3b). Conversely, optogenetic activation of optoATV− was capable of excluding Disp1 from filopodia (Fig. 3c, e). The activated optoATV+ also enabled the transport of MyoXtail-eGFP to the cell membrane, thereby creating new filopodia in Cos7 cells, which normally do not have filopodial extensions (Extended Data Fig. 6 and Supplementary Video 4). In conclusion, optoATVs can achieve targeted manipulation of cellular extensions with high spatiotemporal resolution in living cells and in combination with selective cargo can both induce the formation of cellular extensions or traffic key proteins to the distal ends of these structures.

Optogenetic manipulation of neuronal transport and neurite development in mouse neurons

With the successful implementations of ATVs in manipulating cargo transport in filopodial extensions, we then reasoned that we could rewire neuronal communications using a similar strategy. It would be especially favorable to test our tools in developing neurons, as they harbor highly dynamic growth cones and neurites that are enriched with actin filaments[10,35]. In order to reproducibly gain experimental access to homogeneous populations of maturing neurons, we developed a protocol to generate induced neuronal (iN) cells from mouse embryonic stem cells (mESCs). In short, mESCs were infected with doxycycline-inducible mNeurog2-expressing vectors and plated in petri dishes to form embryoid bodies (EBs). The cells were subsequently replated into neuronal growth media supplemented with doxycycline to differentiate them into iN cells (Fig. 4a). We could consistently generate maturing iN cells that express pan-neuronal markers, such as Tuj1 and MAP2, as early as 5 days of differentiation and the cells continued to mature over 14 days (Extended Data Fig. 7).

We first expressed ATV+ and ATV− in iN cells to examine the localization of these engineered motors. As expected, ATV+ accumulated at peripheral tips of the neurites, while ATV− existed diffusively in the cell body and only excluded from the peripheral neurites (Fig. 4b). Notably, ATV+ could be observed at distal neurite tips up to 100 μm away from the cell body, hence the high processivity of ATV+ is highly useful for long range transport in neurons. We then tested whether we could retract the outgrowth of neurites by trapping MyoXtail-eGFP inside the cell body using ATV−. Indeed, co-expression of MyoXtail-eGFP and ATV− significantly decreased the neurite density by ~8 fold (Fig. 3d, from 46.7 ± 4.6 mm^{-1} to 5.8 ± 0.9 mm^{-1}). Interestingly with the depletion of neurites, the neurons displayed a less mature morphology resembling fibroblasts (Fig. 4c, d). Lastly, we wanted to examine

the efficacy of cargo transport with optoATV+ within neurons. As neuronal mitochondria have a very specialized localization and function[36,37], it was intriguing to test whether optoATV+ could alter the localization of mitochondria in iN cells to influence their function. After short pulses of blue light were applied to the cells co-expressing optoATV+ and the mitochondrial outer membrane targeting signal TOM20-eGFP[38], a significant portion of imaged mitochondria migrated along neurites towards the periphery and neurite spines within 2 minutes (Fig. 4e, f). These results demonstrate that engineered motors are well suited for manipulating cargo transport, including organelles and to directly manipulate neurite development in neurons.

An extensive filopodial network is established during axolotl limb regeneration

A major advantage of ATVs is the ability to specifically manipulate cellular protrusions within dense cellular networks in living organisms *in vivo*. Regeneration is a process that has been reported to mimic normal embryonic development[39], however the importance of filopodial extensions has not yet been investigated in this context. Here, we imaged the axolotl, a classic model system for tissue regeneration, at high spatial resolution *in vivo*, to investigate the role of filopodia in limb patterning during regeneration. In the axolotl, a blastema is formed at the site of limb amputation after the first few days and consists of the progenitor cells that will eventually differentiate to give rise to a newly formed limb[40]. First, we refined a live imaging scheme to conduct confocal imaging at the site of blastema formation in axolotls to obtain high-resolution imaging of the regeneration process *in vivo* (Fig. 5a). Approximately two thirds of the blastema cells were highly efficiently electroporated based on a comparison with Hoechst staining (Extended Data Fig. 8). At 3 days post amputation (dpa), the majority of cells in the blastema region displayed a dedifferentiated morphology with a few cellular protrusions (Fig. 5b). Strikingly, at 7 dpa, an extensive network of filopodia formed in the same region (Fig. 5c). The filopodia that developed share a very similar morphology with the specialized filopodia present in mesenchymal cells during early stages of limb bud development[2], with observed lengths of up to 80 μm (Fig. 5d, e). Notably, no similar filopodia extensions were observed at 3 dpa, indicating a gradual growth of filopodial networks during tissue regeneration (Fig. 5e, from 11.9 ± 0.6 μm to 37.3 ± 1.4 μm). We also electroporated both high-affinity F-actin probes utrophin calponin homology domain fused to eGFP (UCHD-eGFP) and LifeAct-iRFP into axolotl blastema to investigate the underlying cytoskeletal structure. Akin to the observations of specialized filopodia during chick limb development[2], we also observe that UCHD-eGFP labels long and slender filopodia, while LifeAct-iRFP only labels the proximal base (Fig. 5f-h). The quantifications of filopodia length from UCHD-eGFP fluorescence images at 3 dpa and 7 dpa also match very well with those quantified from pmKate2 (Fig. 5f and Extended Data Fig. 9).

In order to study the biological significance of filopodial networks within the axolotl blastema, we set out to manipulate filopodia dynamics utilizing the MyoXtail domain at 3dpa. After co-electroporation of optoATV+ and MyoXtail-eGFP into the blastema, we observed ~2 fold elongation of native filopodia after short pulses of blue light activation at the single cellular level (Fig. 6a, b, from 10.0 ± 2.2 μm to 19.9 ± 3.8 μm). Similarly, the expression of optoATV− and MyoXtail was sufficient to reduce the filopodia density by ~8

fold when 24 hours of ambient room light was provided to the axolotls (Fig. 6c, d, from 18.9 ± 1.0 mm^{-1} to 2.3 ± 0.6 mm^{-1}). Strikingly, while axolotls with retracted filopodia were able to fully regenerate the anterior region of the limb, there was a selective defect in the development of posterior digits at 35 dpa (Fig. 6e). Bone staining showed that cartilage development was severely delayed in the regenerated limb, with almost no staining visible in the posterior region (Fig. 6e). Importantly, with our optogenetic motors, we were able to control the degree of filopodia retraction simply by changing the light-dark cycle of the animals. With a supply of 12 hours light and 12 hours dark per day to the animals, there was a moderate defect in regeneration of the posterior digits compared to when consistent light or dark was supplied, as quantified by the length ratio of digit 3 against digit 1 (Fig. 6e, f, Extended Data Fig. 10a, decreasing from 1.02 ± 0.05 to 0.80 ± 0.05 to 0.23 ± 0.03). Providing consistent light or dark did not affect the selective regeneration of the posterior digits in axolotls electroporated with pmKate2 alone (Extended Data Fig. 10b). These results strongly suggest that filopodia may have a critical role in pattern formation during limb regeneration, and the degree of filopodia retraction is directly correlated with the severity of the posterior digit defect.

A filopodial network is required for Sonic Hedgehog (Shh) signaling during regeneration

The selective posterior digit phenotype suggests a possible involvement of Shh signaling in this process, which is normally required for the development and patterning of posterior digit identities[41]. During axolotl limb regeneration, Shh has also been shown to be critical as inhibition of the pathway by cyclopamine leads to severe digit loss in the regenerated limb[42]. In order to perturb Shh signaling, we performed a proof-of-principle experiment to test whether the key Shh regulator Disp1, could be trafficked with optoATVs *in vivo* to increase Shh release. Similar to the observation in cell culture, we observed that Disp1-eGFP normally localized at patchy regions along filopodial extensions with a slight tendency to accumulate at the tips *in vivo* (Fig. 7a). When optoATV+ was co-electroorated with Disp1-eGFP into the blastema at 3 dpa, Disp1-eGFP was significantly enriched at filopodia tips after brief blue light stimulation (Fig. 7a, b). Conversely, light-activated optoATV− could also efficiently deplete Disp1-eGFP from filopodial extensions within a few minutes (Fig. 7c, d). The kinetics and efficiency of optoATV motors were very similar to those measured in cell culture, indicating that the light activation was highly efficient within dense tissue *in vivo*.

Finally, we conducted quantitative reverse transcription-PCR (RT-qPCR) to quantify the activation pattern of different signaling pathways. We were especially interested in the anterior-posterior axis as the phenotype upon filopodia retraction was largely detected in the posterior region. Therefore, we microdissected the blastema tissue into two equal pieces of anterior and posterior regions for RT-qPCR respectively. Despite the low spatial resolution of this approach, we could observe a significant decrease in the Shh signaling activation level when filopodia were retracted by co-expressing optoATV− and MyoXtail (Fig. 7e, downstream targets *Gli1*: from 7.7 ± 0.4 to 1.1 ± 0.2 fold activation; *Ptch1:* from 5.3 ± 0.1 to 2.4 ± 0.2 fold activation). The co-expression of optoATV+ and Disp1, though, was not significant in increasing Shh activation in the anterior region (Fig. 5e), indicating that Disp1-mediated Shh release may be saturated and the limiting factors may instead be Shh

production or Shh reception. Other pathways such as Wnt5a and Bmp2 did not show significant differential expression between the anterior and posterior regions (Fig. 7e). In conclusion, our studies employing optoATV have led to a functional characterization of a filopodial network and suggest that this network is required for Shh signaling to establish correctly patterned digits during limb regeneration.

Discussion

With recent advents in controlling the localization and function of cellular machineries using induced heterodimerization, it is now feasible to control organelle transport by recruiting them onto native motor proteins using the light-sensitive interaction between LOV and ePDZb1, or the small-molecule dimerizer Zapalog[43,44]. Essentially, either chemical or light stimulation is applied to induce the physical interaction between the target protein and a tagged, actively moving motor protein to achieve cargo movement. Though proven useful, these approaches are all based on native motor proteins that are not ideal in terms of velocity and processivity: most natural myosin motors are too slow and non-processive for the purpose of long-range trafficking. In addition, these native motors also receive internal inputs from cells through extensive modifications[45], which may hinder their utility. There are additional challenges associated with over-expressed motors constitutively moving along the cytoskeletal network, which may cause additional force generation and cellular stress. It has also been impossible to deplete cargo within cellular protrusions using natural minus-ended motors as they are not present in the protrusions[13].

To overcome these obstacles, we have successfully engineered non-natural, fast, processive and optogenetically controlled motor proteins. We show that engineered myosin motors can walk along the actin cytoskeleton in living cells and by appending them with GBP and Cry2olig, we were able to control cargo transport inside cellular extensions with high spatiotemporal resolution. Despite previous attempts of targeting cargo into cellular protrusions[43,46], our results demonstrate successful optogenetic control of cargo transport by processive myosin motors bidirectionally in living cells and organisms.

Notably, ATVs are highly modular, and therefore would be compatible with variant motor arms design to suit for different applications. Hence we envision these tools to be broadly applicable for the cell biology community. Such a tool could be easily extended to other cellular extensions such as cellular projections present on macrophages[4], invadopodia in tumor metastasis[5], and neurites in neurogenesis. In addition, this toolbox enables the direct manipulation of long-range cellular-based communication across many organs and tissues as well as organoids wherein tissue development can be characterized *ex vivo*[47]. In particular, how selective proteins act at a distance, how cells communicate at a long range, and the possibilities for directed manipulation of cellular communication to understanding fundamental principles of organogenesis, are critical areas that would benefit from the development of new tools to manipulate cellular extensions and cell-to-cell communications.

Ethics statement

All animal experiments were performed in compliance with the guidelines for the welfare of experimental animals issued by the Government of the United States. All animal

experiments were approved by Stanford University's Administrative Panel on Laboratory Animal Care.

Plasmid expression constructs

All constructs were expressed using the PBX or PBTREX (for dox-inducible expression) vectors allowing PiggyBac-based transposition[2]. For constitutive expression, full length coding sequences (CDS) were expressed under the CAG promoter (CMV enhancer with chicken beta-actin minimal promoter) allowing strong expression in all cell types tested. For doxycycline-inducible expression, a modified TetOn-3G enhancer minimal promoter element (Clontech) replaced the CAG cassette of PBX to generate PBTREX. The artificial tetrameric plus-ended and minus-ended motors were based on $M6DI_{816}2R$-TET (minus-ended) and $CM11CD_{746}$~1R~TET (plus-ended) as described in a previous publication[15]. The GFP binding protein (GBP) CDS was a gift from R. Parton[48] (Addgene plasmid #67651). ATV+ and ATV- were generated by cloning the GBP at the C-terminus of the plus- and minus- ended motors (flexible linker added in between). OptoATVs were generated by swapping the constitutive GCN4 tetramerization domain of ATVs by the light sensitive Cry2olig domain. Cry2-mCherry CDS was a gift from C. Tucker[33] (Addgene plasmid #60033).

The wild type Patched 1 CDS was a gift from J. Reiter. The stabilized mouse Patched 1 (sPtch1) CDS was generated by truncating the wild type Patched 1 after the 12^{th} transmembrane domain to reduce ubiquitin-based degradation. The mouse Dispatched 1 CDS was purchased from Origene. The myosin X tail domain CDS was a gift from R. Cheney[29]. The human Espin1 CDS was a gift from B. Kachar[28]. Activated mouse mdia2 mutant (mdia2M/A) was created by mutating M into A at the position 1041 to release the autoinhibition in the DAD domain[31]. TOM20-eGFP was generated from the Addgene plasmid #120173. Membrane-bound palmitoylated fluorescent proteins (pmBFP, pmKate2 and pmiRFP) were previously generated in our lab by adding a 20 amino acid sequence of the rat GAP-43 (MLCCMRRTKQVEKNDEDQKI) to the N terminus of each fluorescent protein[2]. UCHD-eGFP and LifeAct-iRFP were also generated in our previous work[2]. The CDS of fluorescent proteins mKate2 (Evrogen), eGFP (Addgene plasmid #18696) and sfGFP[49] (Addgene plasmid #54519) were PCR amplified from representative expression vectors. Individual parts of the constructs were first cloned using the KAPA HiFi PCR kit (Roche) and then assembled using the NEBuilder® HiFi DNA assembly cloning kit (New England Biolabs). The nucleotide sequences of newly generated constructs are attached as supplementary materials.

Cell culture experiments

Cos7 cells (ATCC® CRL-1651™), C3H/10T½ (ATCC® CCL-226™) and HEK293T cells (ATCC® CRL-11268™) were maintained in high glucose DMEM media (Gibco 11965–092), supplemented with 10% FBS (Hyclone), and penicillin–streptomycin mix (GIBCO) at 37 °C with 5% CO_2. The cell lines were purchased from ATCC and only maintained and used within 15 passages to prevent cell morphology changes. The doxycycline-inducible cell lines were cultured with the same media, substituting FBS with the Tet-System Approved FBS (Clontech) that only contained trace amount of tetracycline. Induction of the TetOn-3G

promoter was achieved by the addition of either 1 or 2 μg/ml of doxycycline solution (Sigma).

Cos7 and C3H/10T½ cells were reversely transfected in glass-bottom 96 well plates (Cellvis P96–1.5H-N) using Lipofectamine 2000 (Life Technologies). Briefly, DNA-Lipofectamine mix was diluted in Opti-MEM (Life Technologies) and aliquoted into each well following the manufacturer's instructions. The cells were then dissociated in antibiotics-free DMEM media and counted using the Scepter™ 2.0 cell counter (Millipore Sigma). For each well, 1×10^4 cells were immediately added onto the DNA-Lipofectamine mix resulting in the transfection of 50–200 ng plasmid per well. For each experiment, 2–4 wells of cells were transfected per condition. Transfection was terminated post 24 hours allowing for strong and mosaic expression required for live imaging by replacing the transfection solution with the FluoroBrite™ DMEM media without phenol red (Thermo Fisher), supplemented with 10% FBS or TeT-System Approved FBS one hour prior to imaging.

For optogenetics experiments, 5×10^3 cells were plated and transfected for 24 hours prior to media change to the FluoroBrite™ DMEM media without phenol red, supplemented with 10% FBS. The cells were then grown in the imaging media for another 24 hours to allow for high expression level of mature motors prior to imaging. For each experiment 2–3 wells were transfected per condition. To provide a high level of light protection, small blocks of Metal Velvet light absorbing foil (Acktar) were cut and pasted to the lid of the 96 well plate to minimize laser reflection. The plate was also wrapped with sterile foil after the media change.

Primary Mouse Glia Culture

The CD1 mice were housed in the animal facility at the Veterinary Service Center (VSC) of Stanford University under standard housing conditions (~20–24°C, ~50% humidity, 12 light/12 dark cycle). Primary CD1 mouse glial cells culture was performed as described[50]. Briefly, newborn postnatal (P0) pups were euthanized by decapitation. The cortex was gently dissected from the brain and digested with papain (Worthington Biochemicals) for 30 min. The digested cells were then dissociated by harsh trituration and plated onto T75 flasks (Thermo Fisher) in high glucose DMEM supplemented with 10% FBS. The cells were passaged upon confluency. The glial cells were ready to use for co-culture within 14 days after dissociation.

Viral construction and lentivirus production

The lentiviral constructs used for generating miNCs included TetO-Neurog2-T2A-Puro/TetO-Neurog2-T2A-Puro-P2A-eGFP and Ubi-rtTA[51]. Lentiviruses were produced as described[50]. HEK293T cells were infected at 70% confluency on 10 cm dishes using poly-ethylenimine with three helper plasmids (5 μg pRSV-REV, 5 μg pMDLg/pRRE and 2.5 μg pVSVg) and 10 μg of the lentiviral vector DNA. The supernatant was collected 46 hr after infection and concentrated by ultracentrifugation at 21000 rpm for 2 hr at 4 °C. The lentivirus was then resuspended in the DMEM media, aliquoted, snap-frozen in liquid N_2, and stored at −80°C for no more than 6 weeks before use. The production and usage of lentivirus were all performed in a dedicated BSL2+ laboratory.

Generation of mouse iN cells from mESCs

The V6.5 mouse embryonic stem cells (mESCs) were maintained under the feeder-free condition in 2i + LIF media (DMEM/F12: Neurobasal = 1: 1 Medium (Invitrogen) supplemented with 2.5% FBS (Hyclone), N2 (Gibco), B27 (Gibco), Glutamax (Gibco), 1000 U/ml leukemia inhibitory factor (LIF, Millipore), 3mM CHIR99021 (Tocris) and 1 mM PD0325901 (Tocris)).

In order to generate iN cells, the mESCs were first dissociated with 0.25% Trypsin-EDTA (Gibco). The dissociated cells were then infected with the lentivirus containing Ubi-rtTA and TetO-Neurog2-T2A-Puro with an optional eGFP-expressing virus, and plated on Matrigel (BD Bioscience)-coated 6-well plates in 2i + LIF media on day −4 at the density of 1×10^5 cells/well. The media was changed daily. On day −2, mESCs were dissociated with Trypsin-EDTA and resuspended in the EB media (DMEM/F12 + Neurobasal Media (Invitrogen), 10% Knockout Serum (Gibco), Penicillin/Streptomycin (Gibco), Glutamax (Gibco)) on petri dishes for 2 days to induce embryoid body (EB) formation. On day 0, the EBs were dissociated with Accutase (Innovative Cell Technologies) and plated on Matrigel-coated 6-well plates at a density of 2×10^5 cells/well in the Neurobasal 1% serum media supplemented with Glutamax, B27, Pen/Strep and FBS. In order to promote maturation, 10 ng/mL GDNF (PeproTech), 10 ng/mL BDNF (PeproTech), 20 ng/mL CNTF (PeproTech), 10 μM Forskolin (Fisher Scientific), 100 μM IBMX (Tocris) and 10 ng/mL human NT-3 (PeproTech) was supplemented in the media. 2 mg/l Doxycyclin (Sigma) was added to induce gene expression and was supplemented in the media during the whole differentiation process. From day1 to day3, the cells were continuously selected with puromycin (2 mg/l, Sigma). On day 3, the cells were dissociated with Accutase and re-plated onto 24-well plates with each well containing one Matrigel-coated coverslip at the density of 2×10^4 cells/well. Glia cells were only co-cultured with iN cells for immunofluorescence experiments. The cells were grown in the Neurobasal media containing 1% serum, with additional 5 μM 5-fluorodexoyuridine (FUDR, Sigma) and 4 μM Uridine (Sigma) if glia cells were co-cultured to inhibit glial cell growth. After day 3, 50% of the media in each well was exchanged every 2 days. 2.5% FBS was added to the culture medium starting on day 10 to support the growth of glia cells. Mature iN cells were assayed by immunofluorescence at day 14, while all live-cell experiments were conducted using maturing iN cells at day 5.

For live-cell experiments, the premature iN cells were first washed with pre-warmed FluoroBrite™ DMEM media without phenol red. Then the coverslip with the cells were picked out carefully using a sterile tweezer and turned upside down into a 35 mm glass-bottom fluorodish (World Precision Instruments) filled with the FluoroBrite™ DMEM media. Proper light protection described before was required for optogenetic experiments.

Immunofluorescence

The iN cells were fixed at either day 5 or day 14 in 4% paraformaldehyde in PBS for 10 min at room temperature, followed by three washes with PBS. The cells were then blocked in 5% goat serum for 1 hr at room temperature. Primary antibodies were applied overnight. Cells were washed in PBS three times on the following day, and then stained with secondary

antibodies for 1 hr. Finally, the cells were washed with PBS, and mounted onto glass slides (VWR) for imaging using Fluoromount-G (SouthernBiotech).

The following antibodies were used in this paper for immunofluorescence: mouse anti-Tuj1 (Covance, 1:1,000), chicken anti-MAP2 (Abcam, 1:500), rabbit anti-SYN1 (synaptic systems, 1:200). Alexa-488- and Alexa-594-conjugated secondary antibodies were purchased from Invitrogen.

TIRF microscopy

All images were collected using a Nikon Eclipse-TI inverted microscope (Nikon) equipped with a PLAN APO-TIRF 100×/1.49 oil immersion objective (Nikon) and the Perfect Focus System for continuous maintenance of focus and a heating chamber maintained at 37 °C with 5% CO_2. sfGFP and mKate2 fluorescence channels were excited with 488 and 568 nm laser lines with paired emission filters (Semrock). Images were acquired with an Andor Neo sCMOS camera controlled with the NiS-Elements software (Nikon). For time-lapse experiments, images were collected continuously, using an exposure time of 200 ms, resulting in 4.9 frame per second.

For localized light activation of optoATV+ in live cells, the 488 nm laser line was applied only to square regions previously specified in the software, while the 568 nm laser line was applied to the whole cell.

Axolotl larvae procedures

White axolotl (*Ambystoma mexicanum*) larvae were purchased from the Ambystoma Genetic Stock Center (AGSC) at the University of Kentucky, and individuals were 2–3 cm in length from snout to tail tip when used for experiments. Axolotl larvae were housed in the animal facility at the Veterinary Service Center (VSC) of Stanford University, and were maintained at 18–22 °C in Holtfreter's solution and fed with either live brine shrimp or fish pellets. Holtfreter's solution for each individual was changed three times every week when feeding was performed. Ambient room light was provided for 12 hours each day except for opotogenetic experiments (the provided light condition was stated in the text). Among replicate experiments, healthy animals of the same arrival date and similar size were used. It was not possible to determine the sex of the axolotl larvae at the stage when experiments were performed and therefore was not taken into account for experimental designs.

Axolotl larvae electroporation and surgery

Anesthesia was performed to each axolotl larva for 6–8 minutes in freshly prepared 0.25 g/L Tricaine (Syndel) solution in pre-chilled Holtfreter's solution at a neutral pH. Anesthetized axolotl larvae were placed on agarose-filled petri dishes and observed under a Leica M80 microscope. The left forelimbs were stretched out and positioned with sterile tweezers to enable injection and the subsequent electroporation.

DNA constructs were previously diluted in Dulbecco's phosphate buffered solution (DPBS, Gibco) to reach a final concentration of 1–2 mg/ml were combined with phenol red solution (Sigma, 0.1 mM final concentration) to aid visualization. A capillary glass microinjection

needle (Drummond) generated by a model 720 needle puller (Kopf) was backfilled with 5 μl of DNA injection solution using a microloader tip. The solution was then pressure-injected (WPI Picopump) into the left forelimb (around 2 mm distal to the elbow joint), to allow fully diffusion of the solution into the distal part of the forelimb. Pre-chilled PBS solution was immediately poured onto the agarose to fully immerse the injected limb. An electrode tweezer (Nepagene) previously submerged in PBS solution was placed on both sides of the injected forelimb, and the distance between the electrodes were fixed at 3 mm apart. The limb was then electroporated by applying three poring pulses of 150 V and 5 ms with 10 ms interval followed by five transfer pulses of 50 V and 50 ms with 950 ms interval. The forelimb was kept in place during the electroporation with a tweezer holding the proximal region of the limb.

The electroporated left forelimb of the axolotl larva was then stretched outwards, and the most distal region of the forelimb (around 2 mm distal to the elbow joint) was amputated using a sterile surgical scalpel (Feather). The axolotl larva was then returned to Holtfreter's solution for recovery.

Live imaging mounting scheme of axolotl blastema

The electroporated axolotl larvae were placed in Holtfreter's solution to recover for at least 3 days before imaging. Prior to animal procedures and imaging, sterile hybrislips (Thermo Fisher) were cut to 0.8 × 0.8 cm in size, and four small particles of Blu-Tack adhesive (Bostik) were manually made and attached to the four corners of the hybrislip. Tweezer was used to ensure firm and even attachment of the adhesive. The hybrislip and a sterile 35 mm glass-bottom fluorodish would then be used for the live confocal imaging.

For the axolotl larva to be imaged, anesthesia was performed for 8–10 minutes in freshly prepared 0.25 g/L Tricaine solution in pre-chilled Holtfreter's solution at a neutral pH. The larva was subsequently placed on its belly inside the fluorodish and major liquid droplets inside the dish were removed. The left forelimb was stretched out by a tweezer, and the prepared hybrislip was then mounted on the blastema region. The least possible force was applied with the tweezer on each corner to mount the hybrislip onto the glass bottom without deforming the blastema. The dish was then filled with additional anesthesia solution to submerge the larva, and the mounted live axolotl blastema would be immediately imaged using confocal imaging. Imaging of the larva never exceeded 30 minutes to minimize the impact of long-term anesthesia on the animal. For optogenetic experiments, the mounting procedure was performed strictly in the dark and a red flashlight headlamp was used to aid visualization. The step-by-step protocol for axolotl electroporation and imaging can be found at the Nature Protocol Exchange[52].

For whole mount nucleus staining, a chunk of blastema tissue (approximately 2 mm in length and width) was cut off by a micro knife (Fine Science Tools) and placed into pre-diluted Hoechst solution (1:500, Invitrogen) and vigorously shaken at 37 °C in dark for 1 hour. The blastema tissue was then washed in PBS and mounted in a fluorodish as described above, and subsequently used for confocal imaging.

Live cell and axolotl confocal imaging

Images were acquired in live cells or live animals using a custom-built inverted spinning disk microscope[2]. A Zeiss Axio Observer Z1 microscope was coupled to the Perkin Elmer UltraVIEW Vox spinning disk confocal microscopy system with an encoded ASI MS2000 motorized piezo stage equipped with a Plan-Apochromat 63×/1.20 water immersion objective (Carl Zeiss microscopy). The UltraVIEW Vox system utilized 405 nm (for BFP), 488 nm (for sfGFP), 561 nm (for mKate and mScarlet) and 640 nm (for iRFP) solid state laser lines paired with emission filters (Semrock) that were specifically selected to minimize crosstalk across various fluorescent proteins (452W25 for BFP, 510W20 for sfGFP, 588W21 for mScarlet, 632W22 for mKate and 692LWP for iRFP). Images were captured in the gain mode of a back-thinned Electron Multiplying CCD (EMCCD) camera (Hamamatsu ImageEM C91003). Acquisition of the images was accomplished with the Volocity Acquisition suite 6.1 (Perkin Elmer) for multichannel time-lapse confocal recordings. The laser power and exposure time were adjusted to minimize phototoxicity during the acquisition. The laser power measured at the entrance of the spinning disk was less than 2.5 mW for all excitation wavelengths. The imaging platform was equipped with a heating chamber maintained at 37 °C with 5% CO_2 for all live cell experiments. The heating and CO_2 supply were turned off during live axolotl experiments.

For optogenetics experiments, a pulse of blue light (488 nm, 10% laser power, 100 ms for live cells and 200 ms for live axolotls) was applied at the frequency stated in the text. The activating blue light was also used for monitoring the movement of the cargo. To minimize pre-activation of the motors, approximately 10 positions per well (for live cells) or 6 positions per blastema (for live axolotls) were chosen based on the expression of mKate2 (561 nm) and multi-point optogenetic recording was performed once per well or per animal. The room was kept in the dark, and the imaging chamber was covered with a black nylon fabric during imaging (Thorlabs).

Alcian blue and alizarin red staining

This protocol was adapted from a previous publication[53]. At 35 dpa, the axolotl larvae were euthanized in 5g/L Tricaine solution at neutral pH. Both left and right forelimbs were then dissected from the larva using sterile tweezers (right forelimb as a non-amputated control). The shoulder blade was included with the limb and the skin was partially removed from the bone during this process. The dissected limb was placed in 95% ethanol (EtOH) at 4 °C and fixed overnight. Then it was washed with three 5-min washes in PBS and dehydrated in 25% and 50% EtOH for 10 min each. The dehydrated limb was then placed in alcian blue solution (Sigma, 7.5 mg alcian blue powder dissolved in 50 ml 80% EtOH-20% acetic acid mix) at 4 °C for overnight staining. The vial was covered with foil for light protection.

On the next day, the limb was washed in 80% EtOH-20% acetic acid mix for 1 hour, 95% EtOH for 10 min, and 1% KOH solution for 10 min. After this process, the limb would become relatively fragile and require additional caution when changing solution. The limb was then placed in alizarin red solution (Sigma, 3.75 mg alizarin red powder dissolved in 50 ml 1% KOH solution) at room temperature for 30 min until the ossified regions became visibly stained. It was then washed in 1% KOH-20% glycerol solution for around one hour,

before being placed in 20% glycerol-PBS mix for long-term storage. The stained bones were imaged in petri dishes filled with 20% glycerol-PBS mix, using a Zeiss SteREO Discovery.V8 microscope.

RT-qPCR for the axolotl blastema

The left forelimbs of the axolotl larvae were amputated as described above. At 10 dpa, the axolotl larvae were euthanized and observed under a Leica M80 microscope. The blastema tissue was carefully handled with a sterile tweezer, and micro-dissected into two equal posterior-anterior halves using a micro knife. The dissected blastema tissue was immediately transferred to separate tubes of pre-chilled Trizol (Thermo Fisher). Thorough pipetting and shaking were performed to dissolve the tissue into the solution. The tissue was directly snap-frozen in liquid nitrogen and then stored in −80 °C for further assays.

For RNA extraction, the samples were first thawed on ice and mixed with 1/5 volume of chloroform (Millipore Sigma). The samples were centrifuged at 12000 g for 10 min. The aqueous phase was carefully collected and mixed thoroughly with 1 volume of ethanol (Rossville). RNA was then extracted from the solution using the RNA Clean & Concentrator-5 kit following the manufacturer's instruction (Zymo Research). Reverse transcription of the extracted RNA was achieved using the iScript™ Reverse Transcription Supermix (Bio-Rad). qPCR was performed using the SsoAdvanced™ Universal SYBR Green Supermix (Bio-Rad), and read out using the CFX384™ Touch Real-Time PCR Detection System (Bio-Rad).

The following primers were used for the qPCR:

Rpl4-F: ACACGCAGAGTTCTGAAGAA

Rpl4-R: TGGCTACCTTGACTTCTTCC

Gapdh-F: AAAAGGTCTCCTCTGGCTATGAC

Gapdh-R: AGGGCTATAAAAGAGCATTATCGAG

Gli1-F: ATATCCCACCTCTGAGACCA

Gli1-R: GAAGGGGCGCCATTTTTATT

Ptch1-F: TGTAGATCTGCTCCAATGCAAAC

Ptch1-R: CTGACCCGGAGTACTTGCAG

Wnt5a-F: AGGCAAGCGTCTCAGATTGT

Wnt5a-R: TTCAATAGCCTGGCTGCTCT

Bmp2-F: TCGTGCAGACTTTGGTCAAC

Bmp2-R: CGTTCTCGTCCAGGTAGAGC

Image and video analysis

Acquired images and videos were processed using the Volocity 6.1 “Visualization and Quantification” Suite (Perkin Elmer) unless otherwise stated. Image stacks were acquired at different depths, and the different depths were combined using maximum intensity projection. Filopodia were identified manually based on the cell morphology delineated by the membrane-bound fluorescent proteins (either pmBFP or pmiRFP) and were required to be at least 2 μm in length unless otherwise stated. The cell border was acquired based on an optimized cell detection program to measure the cell perimeter. The activation of optoATV+ was evaluated based on the number of bright optoATV+ puncta at protrusion tips, using a built-in spot identification program. The colocalization index between different channels was obtained using a built-in analysis tool with automatic thresholding. The transportation of cargo was evaluated based on the change of cargo fluorescence intensity at the tip. The fluorescence intensity was further deducted with the measured background fluorescence intensity. For the velocity characterization from TIRF imaging, lines were manually drawn from the cell body to the filopodia tips to generate kymographs using built-in tools in Volocity. The velocity was calculated from the kymographs. The half-time analysis was based on either linear regression for activation (R^2 = 0.9951), or one-phase decay (R^2 = 0.9917) for deactivation. The pseudocolor-coded images based on the z depth were generated from the built-in “Temporal-Color” tool in ImageJ (NIH).

All the recorded values were then exported into Prism 8.4 (GraphPad) for subsequent quantification, data presentation and statistical analysis.

Statistics and reproducibility

Each experiment was performed at least three times independently. Measurements from the different replicates were recorded in Microsoft Excel Version 2010. The significance level was determined using Prism 8.4, assuming non-Gaussian distribution and unequal variance between groups. Specific tests were indicated in representative figure legends. Graphs are shown as mean ± SEM unless otherwise stated.

Reporting Summary

Further information on research design is available in the Nature Research Reporting Summary linked to this article.

Data availability statement

All source data is provided in the supplementary material. Other supporting data of this study is available upon request to the corresponding author.

Extended Data

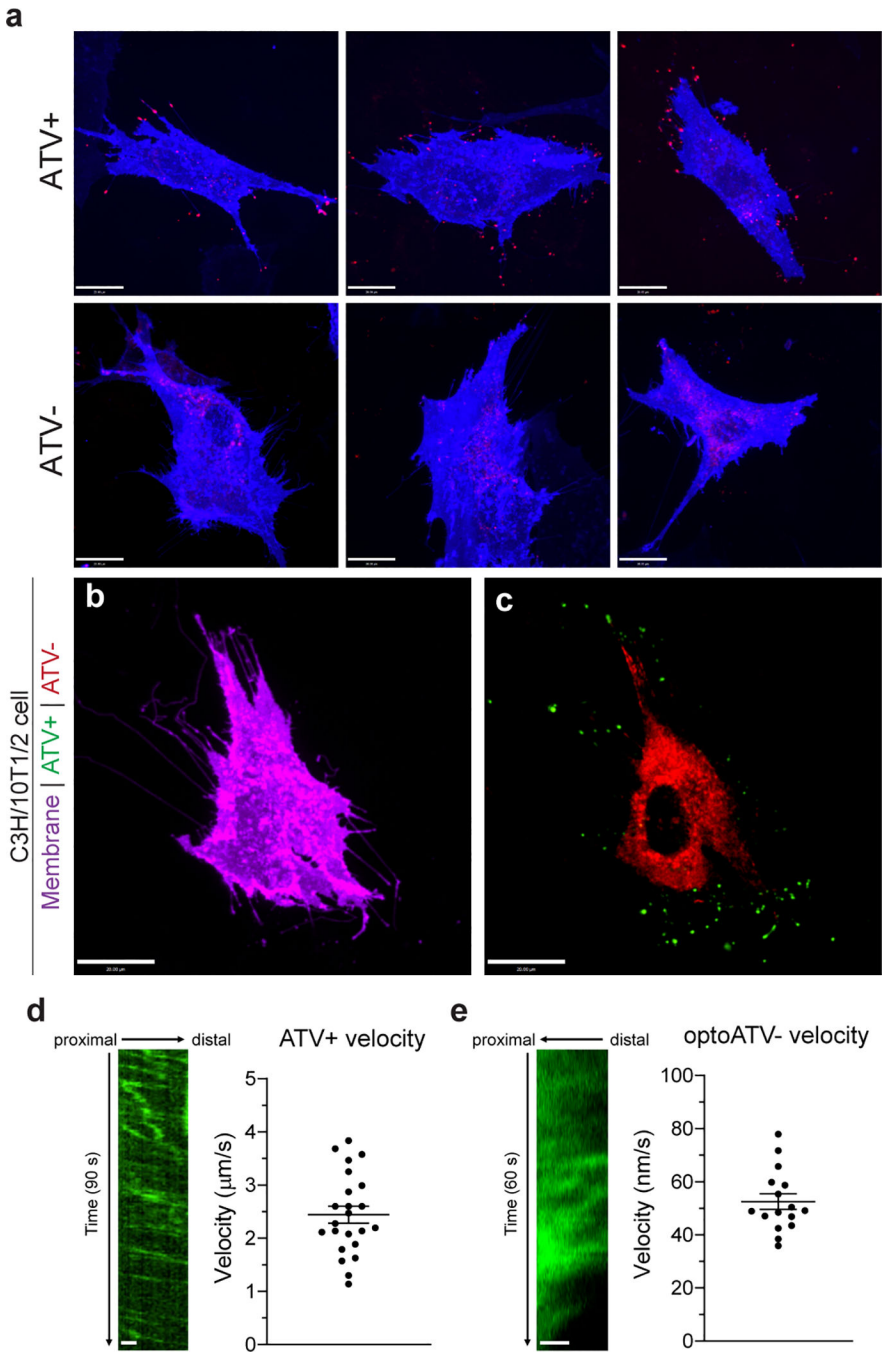

Extended Data Fig. 1. Characterization of ATV+ and ATV− in live cells.

(a) Representative images of randomly chosen mouse fibroblasts expressing either (upper) ATV+ or (lower) ATV− with pmBFP chosen from 3 independent experiments. Scale, 20 μm. (b, c) Mouse fibroblasts co-expressing sfGFP-ATV+, mKate2-ATV− and pmiRFP in the same cells. ATV+ and ATV− display significantly different localization patterns within the same cells. Representative images chosen from 3 independent experiments. Scale, 20 μm. Mouse fibroblasts expressing (d) sfGFP-ATV+ or (e) sfGFP-optoATV− were imaged under

a total internal reflection (TIRF) microscope. (d) Left: A kymograph of a cellular protrusion showing single molecule traces of sfGFP-ATV+ moving down the tip. Scale, 1 μm. Right: Quantification of the velocity of ATV+ moving within cellular protrusions. Single dots represent single molecule traces chosen from 3 independent experiments (N = 23 traces). (e) Left: A kymograph of a cellular protrusion where single molecule traces of sfGFP-optoATV − retracting back to the cell body upon light stimulation. Scale, 100 nm. Right: Quantification of the velocity of activated optoATV− moving within cellular protrusions. Single dots represent single molecule traces chosen from 3 independent experiments (N = 16 traces). The graphs are shown as mean ± SEM.

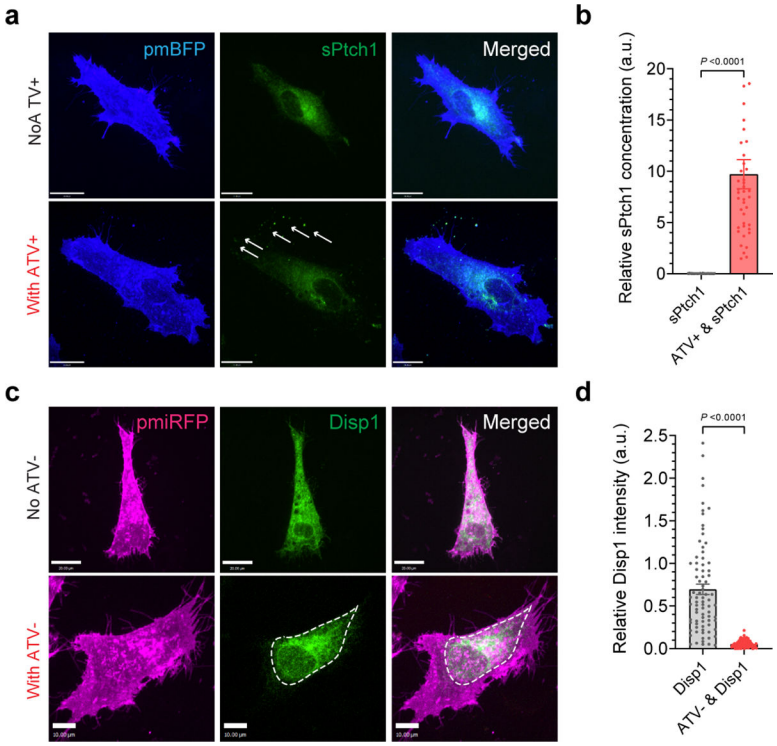

Extended Data Fig. 2. Bidirectional transport of bulky transmembrane SHH receptors within filopodia using ATVs in live cells.

(a) Expression of sPtch1-eGFP with or without co-expression of mKate2-ATV+ in C3H/10T½ cells. Representative images chosen from 3 independent experiments. Scale, 20 μm. (b) Quantification of the relative concentration of sPtch1-eGFP at the tip compared to the cell body (N = 33 and 41 filopodia each), based on images from (a). (c) Expression of Disp1-eGFP with or without co-expression of mKate2-ATV− in C3H/10T½ cells. Representative images chosen from 3 independent experiments. Scale, 20 μm. (d) Quantification of the relative concentration of Disp1-eGFP at the tip compared to the cell body (N = 86 and 96 filopodia each), based on images from (c). Statistics determined by two-tailed Mann-Whitney test. Both bar graphs displayed as mean ± SEM.

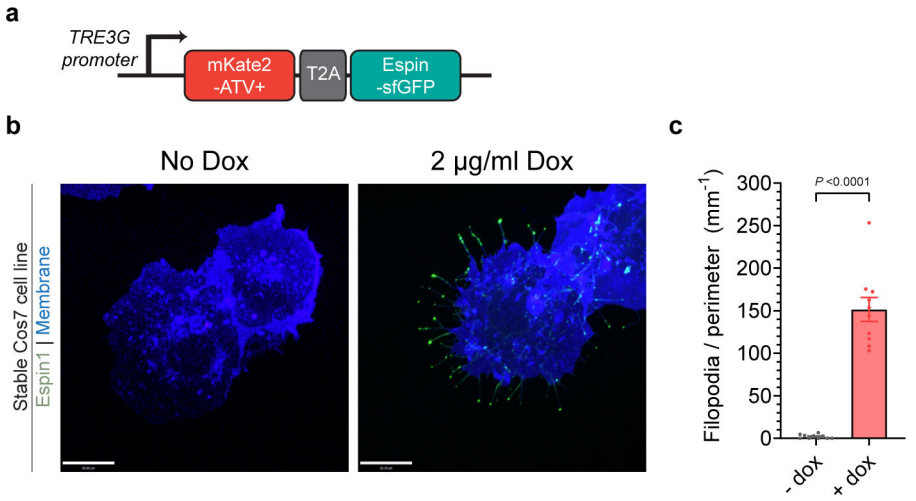

Extended Data Fig. 3. Inducing filopodia growth by doxycycline in a stable Cos7 cell line.

(a) A Cos7 cell line stably expressing mKate2-ATV+ and Espin1-sfGFP (linked with a T2A linker) under a TetOn- 3G system was generated. (b) The cells were imaged with or without 24 hours of 2 μg/ml doxycycline induction. Filopodia growth was only observed when doxycycline was applied. Representative images chosen from 3 independent experiments. Scale, 20 μm. pmBFP was used to visualize full cell morphology. (c) Quantification of the filopodia density of each individual cell (N = 10 cells each). Statistics determined by two-tailed Mann-Whitney test. The bar graph displayed as mean ± SEM.

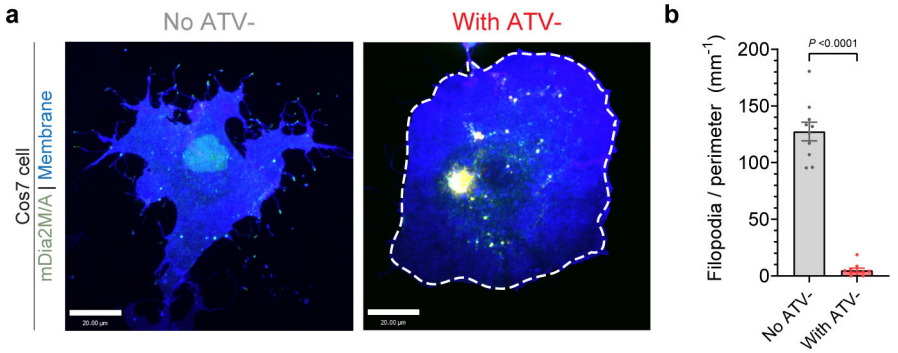

Extended Data Fig. 4. Preventing the outgrowth of mDia2M/A-mediated artificial filopodia using ATV− in live cells.

(a) Expression of sfGFP-mDia2M/A with or without co-expression of mKate2-ATV− in Cos7 cells. The mutant actin nucleating protein mDia2M/A could generate artificial filopodia, while mDia2M/A trapped inside the cell body by mKate2-ATV− could not. Representative images chosen from 3 independent experiments. Scale, 20 μm. (b) Quantification of the filopodia density of each individual cell (N = 10 cells each). Statistics determined by two-tailed Mann-Whitney test. The bar graph displayed as mean ± SEM.

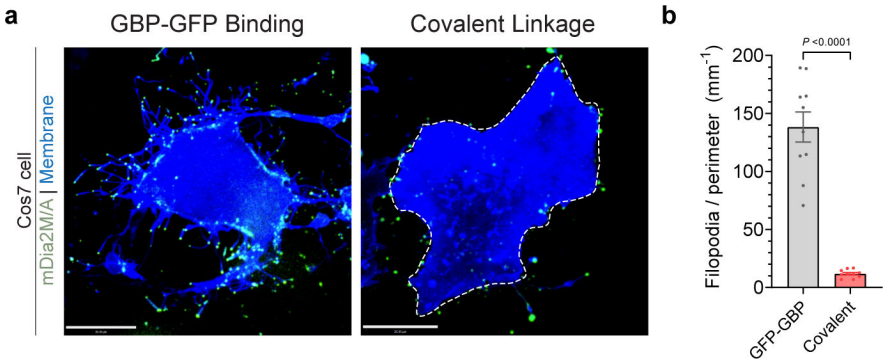

Extended Data Fig. 5. GBP-GFP interaction is necessary for preserving native function of the transported cargo in live cells.

(a) Expression of mKate2-ATV+ & sfGFP-mDia2M/A independently or the covalently linked cargo-motor in Cos7 cells. The prior is based on the binding interaction of GBP-GFP while the latter is based on covalent linkage. GBP-GFP interaction preserved the function of mDia2M/A in generating filopodia, while covalently linkage disrupted cargo function and cells formed fewer filopodia. The white dashed line delineates the smooth cell border. Representative images chosen from 3 independent experiments. Scale, 20 μm. (b) Quantification of the filopodia density of each individual cell (N = 10 cells each). Statistics determined by two-tailed Mann-Whitney test. The bar graph displayed as mean ± SEM.

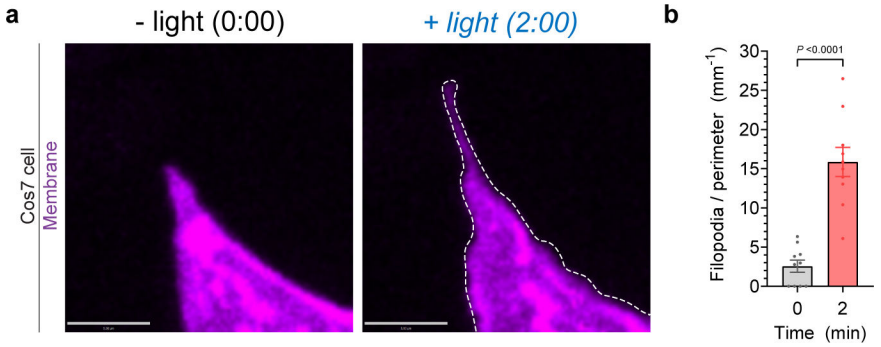

Extended Data Fig. 6. OptoATV+ could generate filopodia *de novo* by transporting MyoXtail to the cell border upon blue light stimulation in live cells.

(a) Expression of mKate2-optoATV+ and eGFP-MyoXtail in Cos7 cells, before and after one pulse of 200 ms blue light every 10 s. *de novo* growth of filopodia could be readily observed after 2 minutes. The white dashed line delineates the cell border where the filopodium was grown. Representative images chosen from 3 independent experiments. Scale, 5 μm. (b) Quantification of filopodia density of each cell before and after light activation (N = 10 cells each). Statistics determined by two-tailed Mann-Whitney test. The bar graph displayed as mean ± SEM.

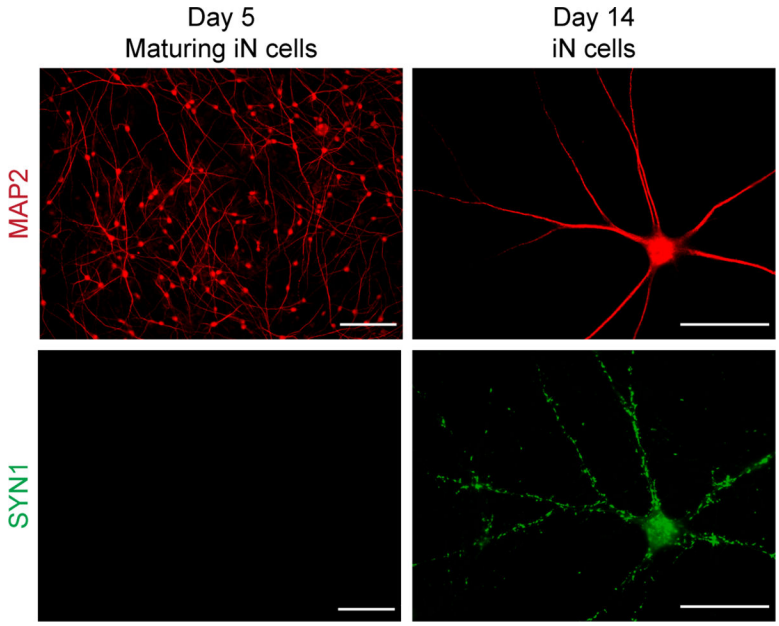

Extended Data Fig. 7. Mouse induced neuronal (iN) cells mature within 14 days of induction.
Immunostaining of maturing iN cells at day 5 (upper lane) or mature iN cells at day 14 (lower lane). Representative images chosen from 3 independent experiments. iN cells readily express the pan-neuronal marker MAP2 at day 5, but only express SYN1 until fully mature at day 14. Scale, 100 μm (upper) or 50 μm (lower).

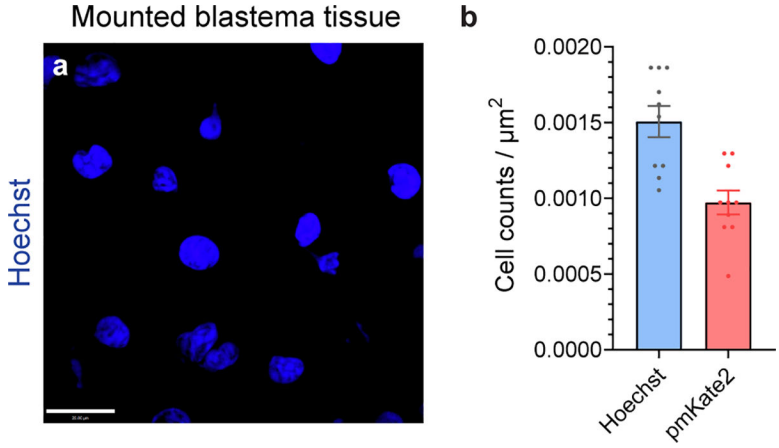

Extended Data Fig. 8. Electroporation is efficient in the axolotl blastema.
Electroporation of the high-affinity F-actin probe utrophin calponin homology domain fused to eGFP (UCHD-eGFP) and LifeAct-iRFP into axolotl blastema. (a) Live imaging of UCHD-eGFP inside axolotl blastema at 3 dpa. Representative images chosen from 3 independent experiments. The z-stack of the images are pseudocolor-coded to show the morphology at different depths. Scale, 20 μm. (b) Histogram plotting the distribution of filopodia lengths at 3 dpa and 7 dpa based on the UCHD-eGFP fluorescence images (N = 63 filopodia each).

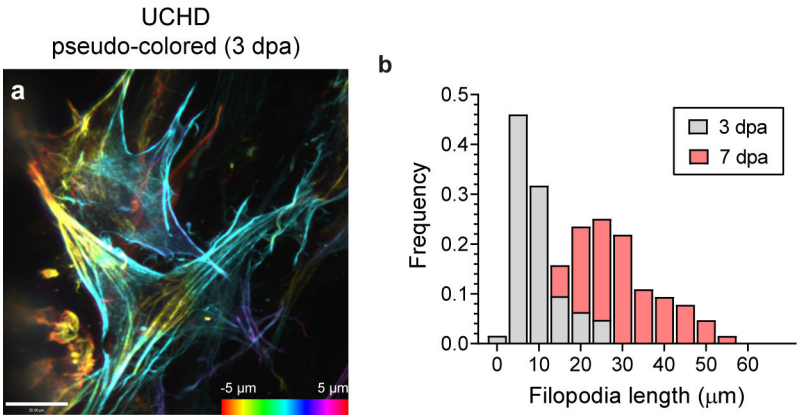

Extended Data Fig. 9. The actin-based filopodial extensions in the axolotl blastema are gradually developed during regeneration.

Electroporation of the high-affinity F-actin probe utrophin calponin homology domain fused to eGFP (UCHD-eGFP) and LifeAct-iRFP into axolotl blastema. (a) Live imaging of UCHD-eGFP inside axolotl blastema at 3 dpa. Representative images chosen from 3 independent experiments. The z-stack of the images are pseudocolor-coded to show the morphology at different depths. Scale, 20 µm. (b) Histogram plotting the distribution of filopodia lengths at 3 dpa and 7 dpa based on the UCHD-eGFP fluorescence images (N = 63 filopodia each).

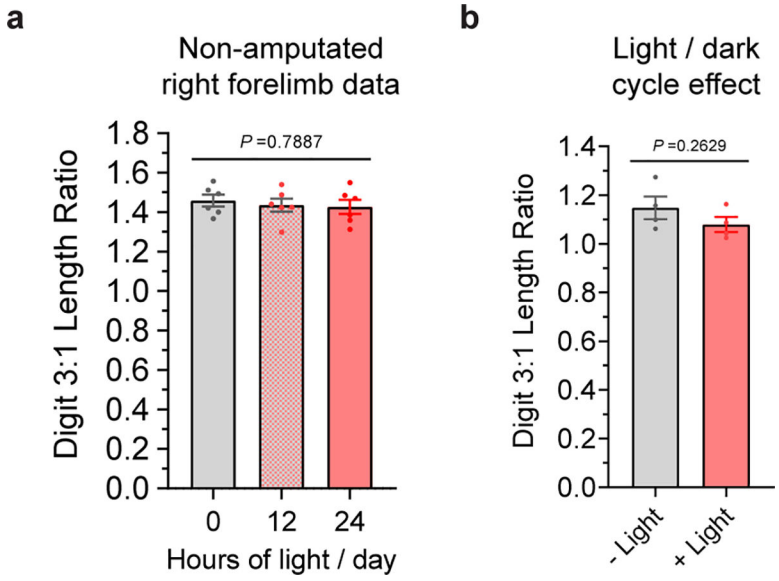

Extended Data Fig. 10. The selective defects in the regenerated posterior digits are not caused by differences in the axolotl background or the light/dark cycle.

(a) Quantification of the non-amputated right forelimb digit length of the axolotls at 35 dpa (N = 6 animals each). (b) Quantification of the regenerated left forelimb digit length ratio of the axolotls that were electroporated with pmKate2 only, with either 0 hour or 24 hours of light provided for 35 days (N = 4 animals each). Statistics determined by two-tailed Welch's ANOVA test or two-tailed *t*-test. Both bar graphs displayed as mean ± SEM.

Supplementary Material

Refer to Web version on PubMed Central for supplementary material.

Acknowledgements

We thank Z. Bryant and P. Ruijgrok for discussion on the design and application of the motors and useful comments on the manuscript, the Cell Sciences Imaging Facility (CSIF) at Stanford University for technical assistance, and the whole Barna Lab for helpful discussion and critical reading of the manuscript. The project described was supported by the Award Number R01HD088597 (M. Barna) and U19MH104172 (M. Wernig) from the National Institutes of Health (NIH), and in part, by Award Number 1S10OD01227601 from the National Center for Research Resources (NCRR). Its contents are solely the responsibility of the authors and do not necessarily represent the official views of NIH or NCRR. Z. Zhang is supported in part by the NIH P50 training grant. O. Zhulyn is a Simons Fellow of the Helen Hay Whitney Foundation (HHWF) and in part supported by the Canadian Institutes for Health Research (CIHR) Fellowship. M. Barna is a New York Stem Cell Foundation (NYSCF) Robertson Investigator and M. Wernig is a Howard Hughes Medical Institute (HHMI) Faculty Scholar.

References

1. Jacquemet Guillaume, Hamidi Hellyeh, and Ivaska Johanna. “Filopodia in cell adhesion, 3D migration and cancer cell invasion.” Current opinion in cell biology 36, 23–31 (2015). [PubMed: 26186729]
2. Sanders Timothy A., Llagostera Esther, and Barna Maria. “Specialized filopodia direct long-range transport of SHH during vertebrate tissue patterning.” Nature 497.7451, 628 (2013). [PubMed: 23624372]
3. Roy S, Hsiung F & Kornberg TB Specificity of Drosophila cytonemes for distinct signaling pathways. Science 332, 354–358 (2011). [PubMed: 21493861]
4. Möller J, Lühmann T, Chabria M, Hall H, & Vogel V Macrophages lift off surface-bound bacteria using a filopodium-lamellipodium hook-and-shovel mechanism. Scientific reports, 3, 2884 (2013). [PubMed: 24097079]
5. Eddy Robert J., et al. “Tumor cell invadopodia: invasive protrusions that orchestrate metastasis.” Trends in cell biology27.8, 595–607 (2017). [PubMed: 28412099]
6. Spector Ilan, et al. “Latrunculins: novel marine toxins that disrupt microfilament organization in cultured cells.” Science219.4584, 493–495 (1983). [PubMed: 6681676]
7. MacLean-Fletcher Susan, and Pollard Thomas D.. “Mechanism of action of cytochalasin B on actin.” Cell 20.2, 329–341 (1980). [PubMed: 6893016]
8. Heimsath Ernest G., et al. “Myosin-X knockout is semi-lethal and demonstrates that myosin-X functions in neural tube closure, pigmentation, hyaloid vasculature regression, and filopodia formation.” Scientific reports 7.1, 17354 (2017). [PubMed: 29229982]
9. Davis Daniel M., and Sowinski Stefanie. “Membrane nanotubes: dynamic long-distance connections between animal cells.” Nature reviews Molecular cell biology 9.6, 431 (2008). [PubMed: 18431401]
10. Matus Andrew. “Actin-based plasticity in dendritic spines.” Science 290.5492, 754–758 (2000). [PubMed: 11052932]
11. Small JV, Isenberg G, and Celis JE. “Polarity of actin at the leading edge of cultured cells.” Nature 272.5654, 638 (1978). [PubMed: 565473]
12. Urban Edit, et al. “Electron tomography reveals unbranched networks of actin filaments in lamellipodia.” Nature cell biology12.5, 429 (2010). [PubMed: 20418872]
13. Vale RD “The molecular motor toolbox for intracellular transport.” Cell 112, 467–480 (2003). [PubMed: 12600311]
14. Howard J “Molecular motors: structural adaptations to cellular functions.” Nature 389, 561–567 (1997). [PubMed: 9335494]
15. Schindler Tony D., et al. “Engineering myosins for long-range transport on actin filaments.” Nature nanotechnology 9.1, 33 (2014).
16. Harbury Pehr B., et al. “A switch between two-, three-, and four-stranded coiled coils in GCN4 leucine zipper mutants.” Science 262.5138, 1401–1407 (1993). [PubMed: 8248779]

17. Rothbauer Ulrich, et al. “Targeting and tracing antigens in live cells with fluorescent nanobodies.” Nature methods 3.11, 887 (2006). [PubMed: 17060912]
18. Sarov Mihail, et al. “A genome-wide resource for the analysis of protein localisation in Drosophila.” Elife 5, e12068 (2016). [PubMed: 26896675]
19. Harikumar Arigela, et al. “An endogenously tagged fluorescent fusion protein library in mouse embryonic stem cells.” Stem cell reports 9.4, 1304–1314 (2017). [PubMed: 28966122]
20. Reznikoff Catherine A., Brankow David W., and Heidelberger Charles. “Establishment and characterization of a cloned line of C3H mouse embryo cells sensitive to postconfluence inhibition of division.” Cancer research 33.12, 3231–3238 (1973). [PubMed: 4357355]
21. Kerber Michael L., et al. “A novel form of motility in filopodia revealed by imaging myosin-X at the single-molecule level.” Current Biology 19.11, 967–973 (2009). [PubMed: 19398338]
22. Bischoff Marcus, et al. “Cytonemes are required for the establishment of a normal Hedgehog morphogen gradient in Drosophila epithelia.” Nature cell biology 15.11, 1269 (2013). [PubMed: 24121526]
23. di Magliano Marina Pasca, and Hebrok Matthias. “Hedgehog signalling in cancer formation and maintenance.” Nature reviews cancer 3.12, 903 (2003). [PubMed: 14737121]
24. Rohatgi Rajat, Milenkovic Ljiljana, and Scott Matthew P.. “Patched1 regulates hedgehog signaling at the primary cilium.” Science 317.5836, 372–376 (2007). [PubMed: 17641202]
25. Gong Xin, et al. “Structural basis for the recognition of Sonic Hedgehog by human Patched1.” Science 361.6402 (2018).
26. Yue Shen, et al. “Requirement of Smurf-mediated endocytosis of Patched1 in sonic hedgehog signal reception.” Elife 3, e02555 (2014).
27. Callejo Ainhoa, et al. “Dispatched mediates Hedgehog basolateral release to form the long-range morphogenetic gradient in the Drosophila wing disk epithelium.” Proceedings of the National Academy of Sciences 10831, 12591–12598 (2011).
28. Salles Felipe T., et al. “Myosin IIIa boosts elongation of stereocilia by transporting espin 1 to the plus ends of actin filaments.” Nature cell biology 11.4, 443 (2009). [PubMed: 19287378]
29. Berg Jonathan S., and Cheney Richard E.. “Myosin-X is an unconventional myosin that undergoes intrafilopodial motility.” Nature cell biology 4.3 246–250 (2002). [PubMed: 11854753]
30. Bohil Aparna B., Robertson Brian W., and Cheney Richard E.. “Myosin-X is a molecular motor that functions in filopodia formation.” Proceedings of the National Academy of Sciences 103.33 12411–12416 (2006).
31. Barzik Melanie, et al. “Ena/VASP regulates mDia2-initiated filopodial length, dynamics, and function.” Molecular biology of the cell 25.17, 2604–2619 (2014). [PubMed: 24989797]
32. Kennedy Matthew J., et al. “Rapid blue-light–mediated induction of protein interactions in living cells.” Nature methods 7.12 973 (2010). [PubMed: 21037589]
33. Taslimi Amir, et al. “An optimized optogenetic clustering tool for probing protein interaction and function.” Nature communications 5, 4925 (2014).
34. Prigozhina Natalie L., and Waterman-Storer Clare M.. “Protein kinase D-mediated anterograde membrane trafficking is required for fibroblast motility.” Current Biology 14.2 88–98 (2004). [PubMed: 14738729]
35. Okabe Shigeo, and Hirokawa Nobutaka. “Actin dynamics in growth cones.” Journal of Neuroscience 11.7, 1918–1929 (1991). [PubMed: 1712377]
36. Sheng Zu-Hang, and Cai Qian. “Mitochondrial transport in neurons: impact on synaptic homeostasis and neurodegeneration.” Nature Reviews Neuroscience 132, 77–93 (2012). [PubMed: 22218207]
37. Hollenbeck Peter J., and Saxton William M.. “The axonal transport of mitochondria.” Journal of cell science 118.23, 5411–5419 (2005). [PubMed: 16306220]
38. Abe Y, Shodai T, Muto T, Mihara K, Torii H, Nishikawa SI, … & Kohda D Structural basis of presequence recognition by the mitochondrial protein import receptor Tom20. Cell, 100(5), 551–560 (2000). [PubMed: 10721992]

39. Imokawa Yutaka, and Yoshizato Katsutoshi. “Expression of Sonic hedgehog gene in regenerating newt limb blastemas recapitulates that in developing limb buds.” Proceedings of the National Academy of Sciences 94.17, 9159–9164 (1997).
40. McCusker Catherine, Bryant Susan V., and Gardiner David M.. “The axolotl limb blastema: cellular and molecular mechanisms driving blastema formation and limb regeneration in tetrapods.” Regeneration 2.2, 54–71 (2015). [PubMed: 27499868]
41. Litingtung Ying, et al. “Shh and Gli3 are dispensable for limb skeleton formation but regulate digit number and identity.” Nature 418.6901, 979 (2002). [PubMed: 12198547]
42. Roy Stéphane, and Gardiner David M.. “Cyclopamine induces digit loss in regenerating axolotl limbs.” Journal of Experimental Zoology 2932, 186–190 (2002).
43. Van Bergeijk Petra, et al. “Optogenetic control of organelle transport and positioning.” Nature 518.7537, 111 (2015). [PubMed: 25561173]
44. Gutnick Amos, et al. “The light-sensitive dimerizer zapalog reveals distinct modes of immobilization for axonal mitochondria.” Nature cell biology 21.6, 768–777 (2019). [PubMed: 31061466]
45. Verhey Kristen J., and Hammond Jennetta W.. “Traffic control: regulation of kinesin motors.” Nature reviews Molecular cell biology 10.11, 765–777 (2009). [PubMed: 19851335]
46. Bird Jonathan E., et al. “Harnessing molecular motors for nanoscale pulldown in live cells.” Molecular biology of the cell 28.3, 463–475 (2017). [PubMed: 27932498]
47. Fatehullah Aliya, Tan Si Hui, and Barker Nick. “Organoids as an in vitro model of human development and disease.” Nature cell biology 18.3, 246–254 (2016). [PubMed: 26911908]

References

48. Ariotti Nicholas, et al. “Modular detection of GFP-labeled proteins for rapid screening by electron microscopy in cells and organisms.” Developmental cell 35.4, 513–525 (2015). [PubMed: 26585296]
49. Pédelacq Jean-Denis, et al. “Engineering and characterization of a superfolder green fluorescent protein.” Nature biotechnology 24.1, 79 (2006).
50. Zhang Yingsha, et al. “Rapid single-step induction of functional neurons from human pluripotent stem cells.” Neuron 78.5, 785–798 (2013). [PubMed: 23764284]
51. Ang Cheen Euong, et al. “The novel lncRNA lnc-NR2F1 is pro-neurogenic and mutated in human neurodevelopmental disorders.” Elife 8, e41770 (2019). [PubMed: 30628890]
52. Zhang Zijian, et al. “Optogenetic manipulation of cellular communication in axolotls.” Protocol Exchange (2020).
53. Nacu Eugeniu, et al. “FGF8 and SHH substitute for anterior–posterior tissue interactions to induce limb regeneration.” Nature 533.7603, 407 (2016). [PubMed: 27120163]

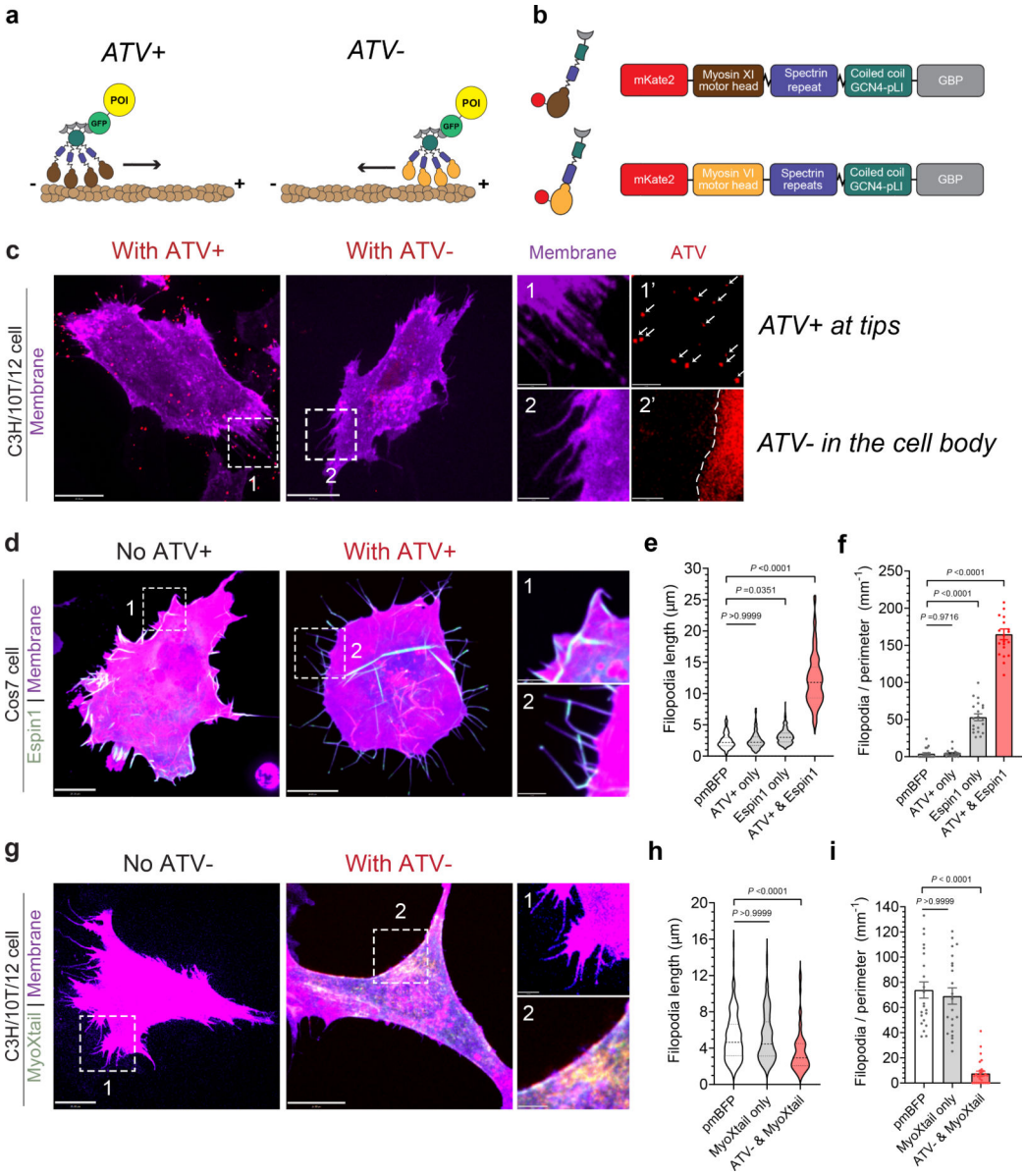

Figure 1. Design, characterization and applications of ATVs in live cells

(a, b) Schematic of movement along actin filaments and constructs of mKate2-ATV+ and mKate2-ATV−. The motors are based on M6DI$_{816}$2R-TET (minus-ended) and CM11CD$_{746}$~1R~TET (plus-ended) as described in a previous publication[15]. Brown filaments represent actin filaments in filopodia. POI: protein of interest.

(c) Expression of mKate2-ATV+ or mKate2-ATV− in C3H/10T½ cells. Representative images chosen from 3 independent experiments. Numbered dashed white boxes of cellular protrusions are magnified on the right, showing the subcellular localization of ATV+ and ATV− with separate channels of the cell membrane. Bright puncta of ATV+ are indicated by white arrows, while the confined localization of ATV− in the cell body is illustrated by the white dashed line. Scale, 20 μm (original) or 5 μm (magnified).

(d-f) Expression of Espin1-super folder GFP (sfGFP) with or without co-expression of mKate2-ATV+ in Cos7 cells. (d) Representative images chosen from 3 independent experiments. Numbered dashed white boxes are magnified on the right. Scale, 20 μm (original) or 5 μm (magnified). (e) Quantification of the length of each filopodia (N = 70, 75, 180 and 235 filopodia each). (f) Quantification of the density of filopodia around the cell border of each individual cell (N = 20 cells each). Statistics determined by two-tailed Kruskal-Wallis test and Dunn's post-hoc test.

(g-i) Expression of enhanced GFP (eGFP)-MyoXtail with or without co-expression of mKate2-ATV− in C3H/10T½ cells. (g) Representative images chosen from 3 independent experiments. Numbered dashed white boxes are magnified on the right. Scale, 20 μm (original) or 5 μm (magnified). (h) Quantification of the length of each filopodia (N = 198, 190 and 58 filopodia each). (i) Quantification of the density of filopodia around the cell border of each individual cell (N = 22, 22 and 30 cells each). Statistics determined by two-tailed Kruskal-Wallis test and Dunn's post-hoc test.

Bar graphs in f,i displayed as mean ± SEM. Violin plots in e,h display the median and quartiles using dotted lines.

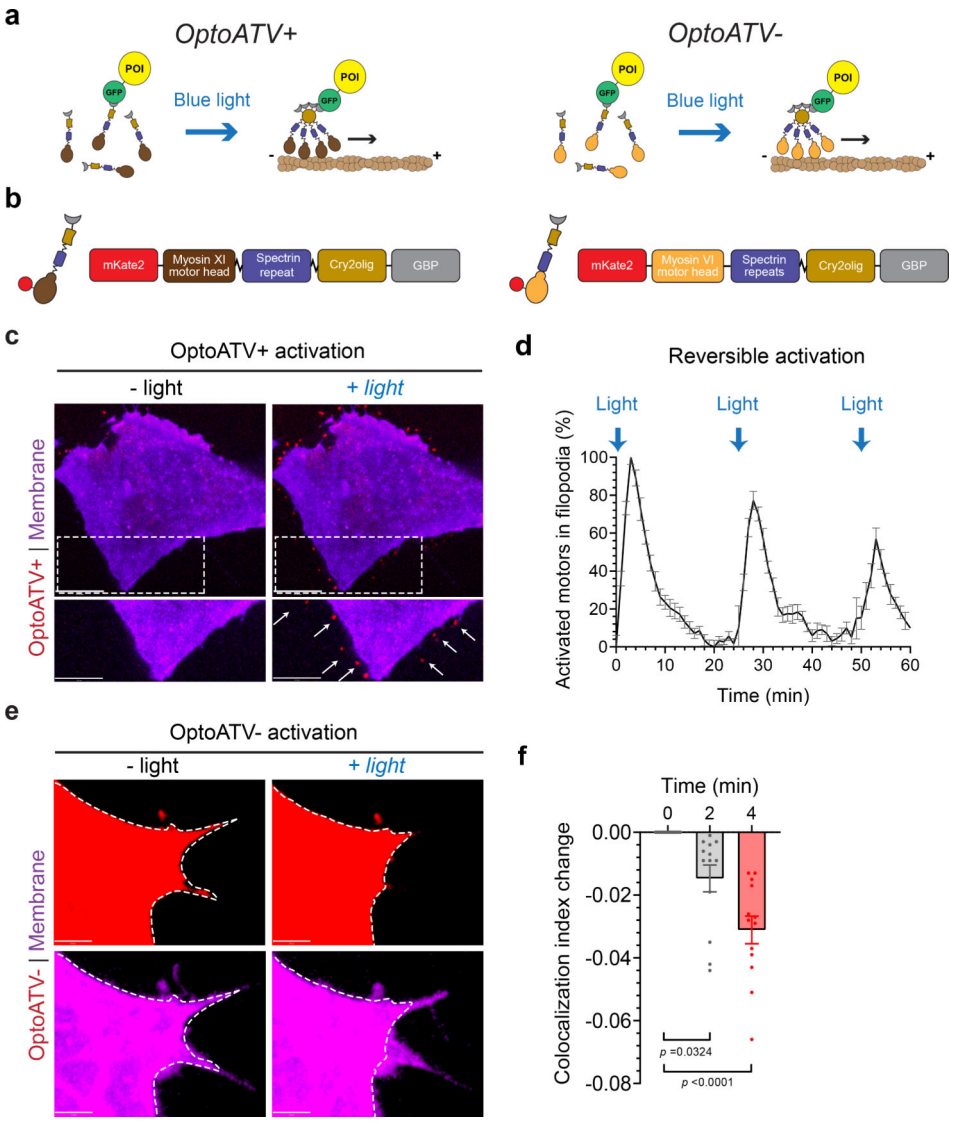

Figure 2. Design and characterization of optoATVs in live cells

(a, b) Schematic of blue light activation and constructs of mKate2-optoATV+ and mKate2-optoATV−. Brown filaments represent actin filaments in filopodia.

(c, d) Expression of mKate2-optoATV+ shows reversible and efficient transportation of the motor to the filopodia tip upon blue light illumination. (d) Representative images chosen from 3 independent experiments. Regions in the white dashed boxes are magnified to show the accumulation of optoATV+ in the filopodia indicated by white arrows. Scale, 15 μm (original) or 10 μm (magnified). (d) Quantification of the reversible activation of optoATV+ by providing one pulse of blue light every 25 minutes (N = 12 cells). Shown is the percentage of activated optoATV+ at filopodia tips normalized by the maximum.

(e, f) Expression of mKate2-optoATV− shows efficient depletion of the motor within filopodia upon blue light stimulation. (e) Representative images chosen from 3 independent experiments. White dashed lines indicate the boundaries of mKate2-optoATV−. Scale, 5 μm. (f) Quantification of the activation level of optoATV− using the colocalization index of iRFP

(membrane) and mKate2 (optoATV−) as the metric (N = 12 cells). Statistics determined by two-tailed Friedman test and Dunn's post-hoc test. The bar graph displayed as mean ± SEM.

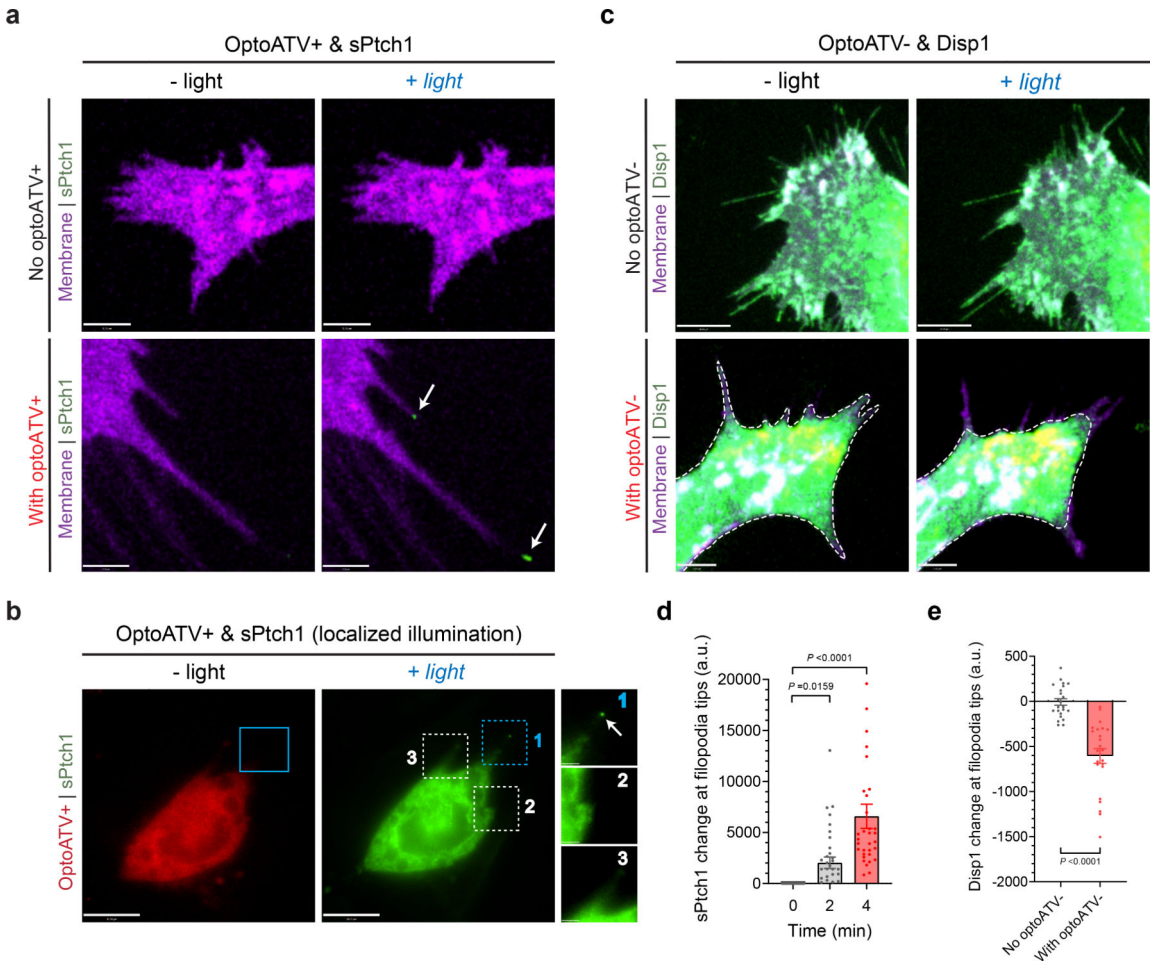

Figure 3. Applications of optoATVs in live cells

(a) Expression of sPtch1-eGFP with (bottom) or without (top) mKate2-optoATV+ in C3H/10T½ cells before and after 5 pulses of blue light within 10 minutes. Representative images chosen from 3 independent experiments. The white arrows indicate the accumulation of sPtch1 at filopodia tips after blue light activation. Scale, 5 μm.

(b) Localized illumination of a cell expressing mKate2-optoATV+ and sPtch1-eGFP. Blue boxes in both figures show the illuminated region, while the white dashed boxes on the right are two non-illuminated regions with filopodia. Accumulation of sPtch1 is indicated by the white arrow. Scale, 10 μm (original) or 2 μm (boxed regions). Representative images chosen from 3 independent experiments.

(c) Expression of Disp1-eGFP with (bottom) or without (top) optoATV− in C3H/10T½ cells, before and after 5 pulses of blue light within 10 minutes. The white dashed line delineates the existence of Disp1 only in the cell body after the light stimulation. Representative images chosen from 3 independent experiments. Scale, 10 μm (upper) or 5 μm (lower).

(d) Quantification of sPtch1-eGFP concentration change at filopodia tips after activation of optoATV+ (N = 36 filopodia). Statistics determined by two-tailed Friedman test and Dunn's post-hoc test.

(e) Quantification of Disp1-eGFP concentration change at filopodia tips after activation of optoATV− (N = 23 filopodia). Statistics determined by two-tailed Mann-Whitney test.

Both bar graphs displayed as mean ± SEM.

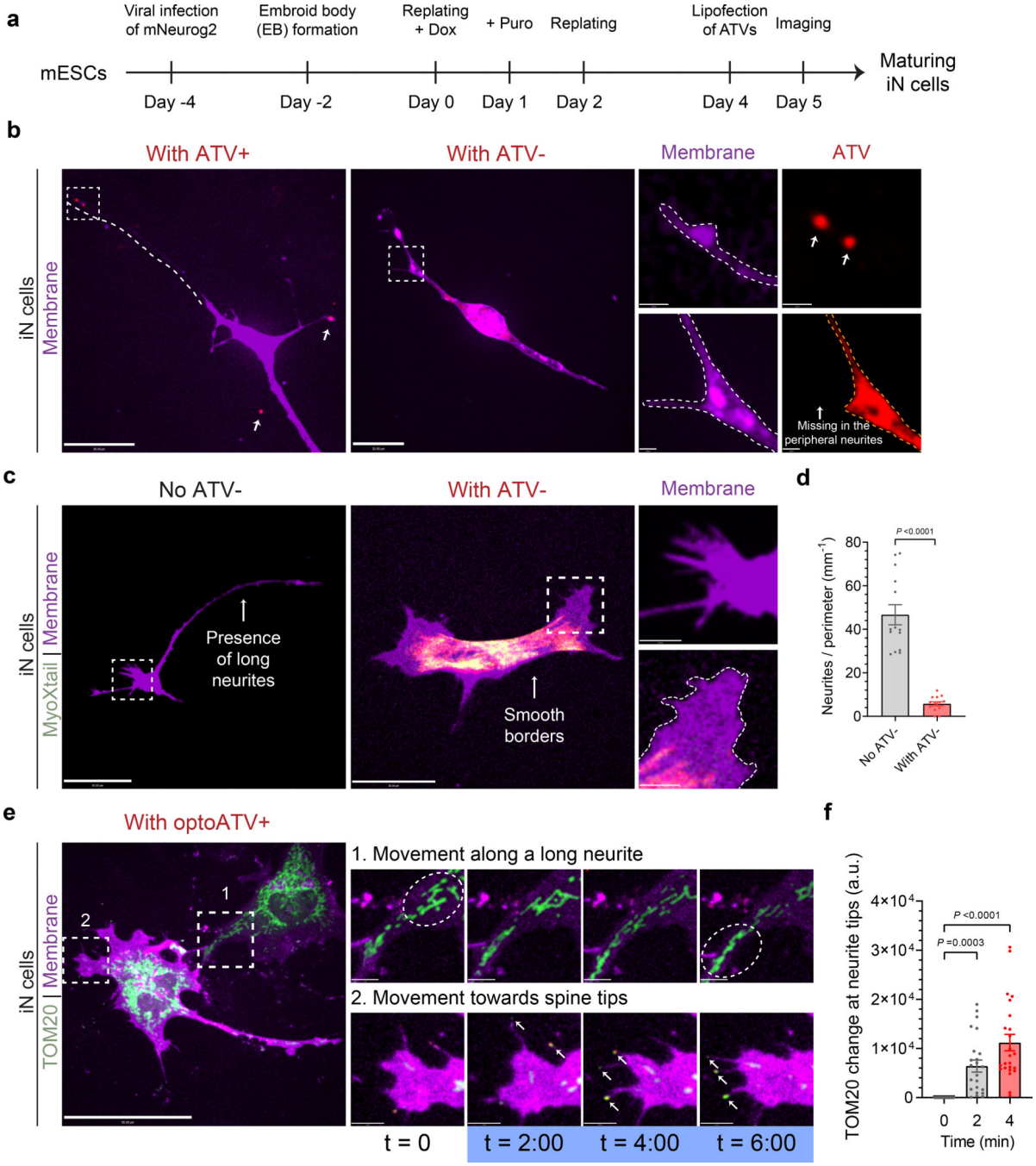

Figure 4. Characterization and applications of ATVs and optoATVs in mouse induced neuronal (iN) cells

(a) Schematic time schedule for the generation of iN cells from mESCs. Day 0 indicates the beginning of Neurog2 expression to initiate differentiation.

(b) Expression of mKate2-ATV+ or mKate2-ATV− in iN cells. Representative images chosen from 3 independent experiments. Numbered dashed white boxes of cellular protrusions are magnified on the right, showing the subcellular localization of ATV+ and ATV− with separate channels of the cell membrane. Bright puncta of ATV+ were pointed by the white arrows, cell membrane border was indicated by the white dashed lines, while the

exclusion of ATV− in peripheral neurites was indicated by the orange dashed line. Scale, 20 μm (original) or 2 μm (magnified).

(c, d) Expression of eGFP-MyoXtail with or without co-expression of mKate2-ATV− in iN cells. (c) Representative images chosen from 3 independent experiments. Numbered dashed white boxes are magnified on the right. Scale, 50 μm (original) or 10 μm (magnified). (g) Quantification of the density of neurites around the cell border of each individual miNCs (N = 14 cells each). Statistics determined by two-tailed Mann Whitney test.

(e, f) Expression of mKate2-optoATV+ and TOM20-eGFP in iN cells shows transportation of mitochondria to the periphery of neurites and spine tips upon blue light illumination. (e) Representative images chosen from 3 independent experiments. Numbered dashed white boxes are magnified on the right to show two different time series of movement. White circled regions highlight the major localization of mitochondria at two different time points; white arrows indicate the accumulation of mitochondria at spine tips. Scale, 50 μm (original) or 5 μm (magnified). (f) Quantification of TOM20-eGFP accumulation at spine tips after light activation (N = 24 neurite spines). Statistics determined by two-tailed Friedman test and Dunn’s post-hoc test.

Both bar graphs displayed as mean ± SEM.

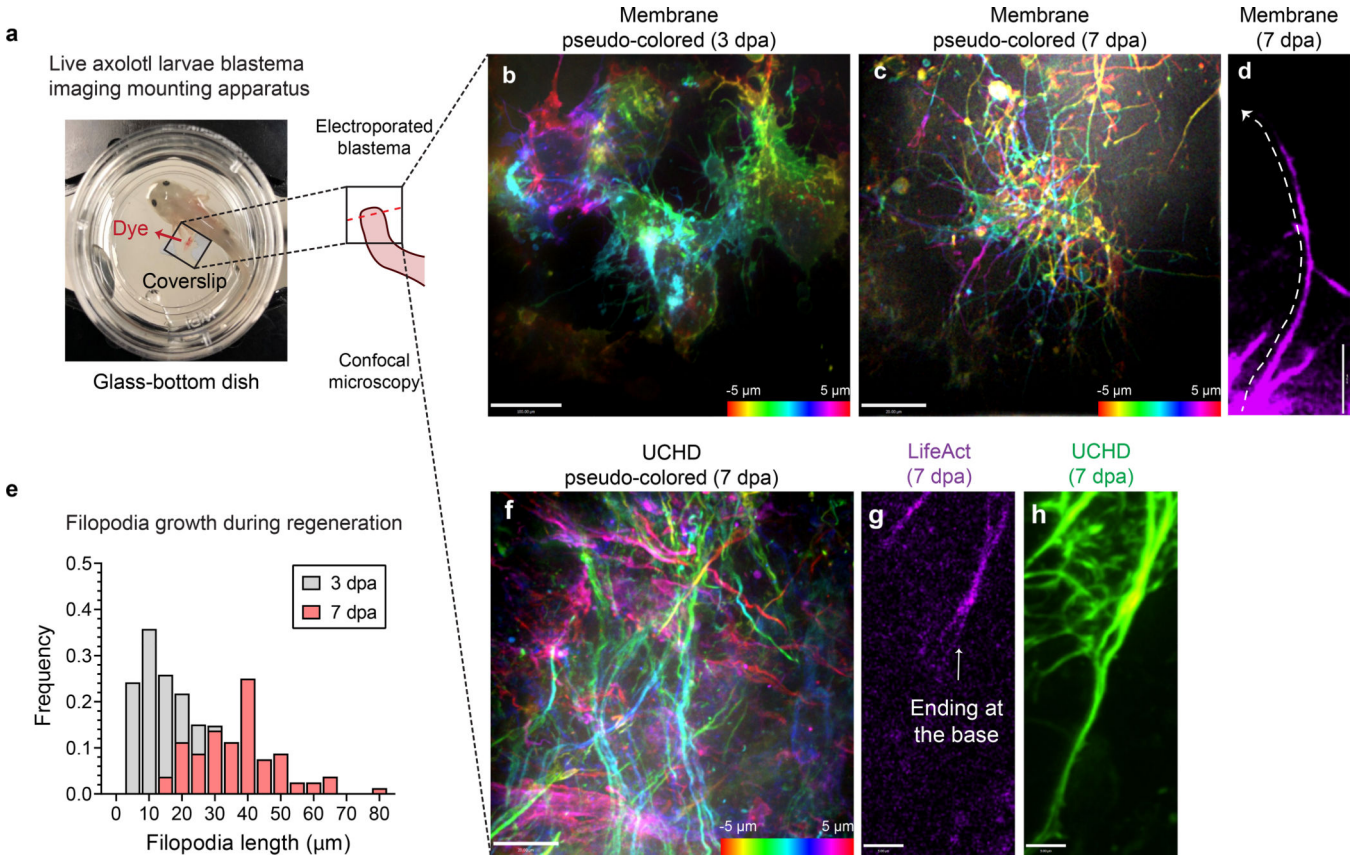

Figure 5. Live confocal imaging reveals the presence of an extensive filopodial network

(a) A representative image showing the setup and mounting apparatus for live imaging on axolotl larvae. Phenol red indicates the region of electroporation. Boxed region is under a plastic hybrislip and enlarged to show the imaging field. The red dashed line represents the site of amputation.

(b-e) Live imaging of axolotl blastema electroporated with a membrane marker pmKate2 at (b) 3 dpa or (c) 7 dpa. Representative images chosen from 4 independent experiments. The z-stack of the images are pseudocolor-coded to show the morphology at different depths. Scale, 20 µm. (d) Cropped image from (c) showing a long filopodia that extends over 70 µm. Scale, 20 µm. (e) Histogram plotting the distribution of filopodia length at either 3 dpa or 7 dpa (95 and 80 filopodia each).

(f-h) Electroporation of the high-affinity F-actin probe utrophin calponin homology domain fused to eGFP (UCHD-eGFP) and LifeAct-iRFP into axolotl blastema. (f) Live imaging of UCHD-eGFP inside axolotl blastema at 7 dpa. Representative images chosen from 3 independent experiments. The z-stack of the images are pseudocolor-coded to show the morphology at different depths. Scale, 20 µm. (g, h) Enlarged view of a single filopodium inside the axolotl blastema at 7dpa. (g) LifeAct-iRFP only labels the base of the (h) UCHD-decorated filopodium. Scale, 5 µm.

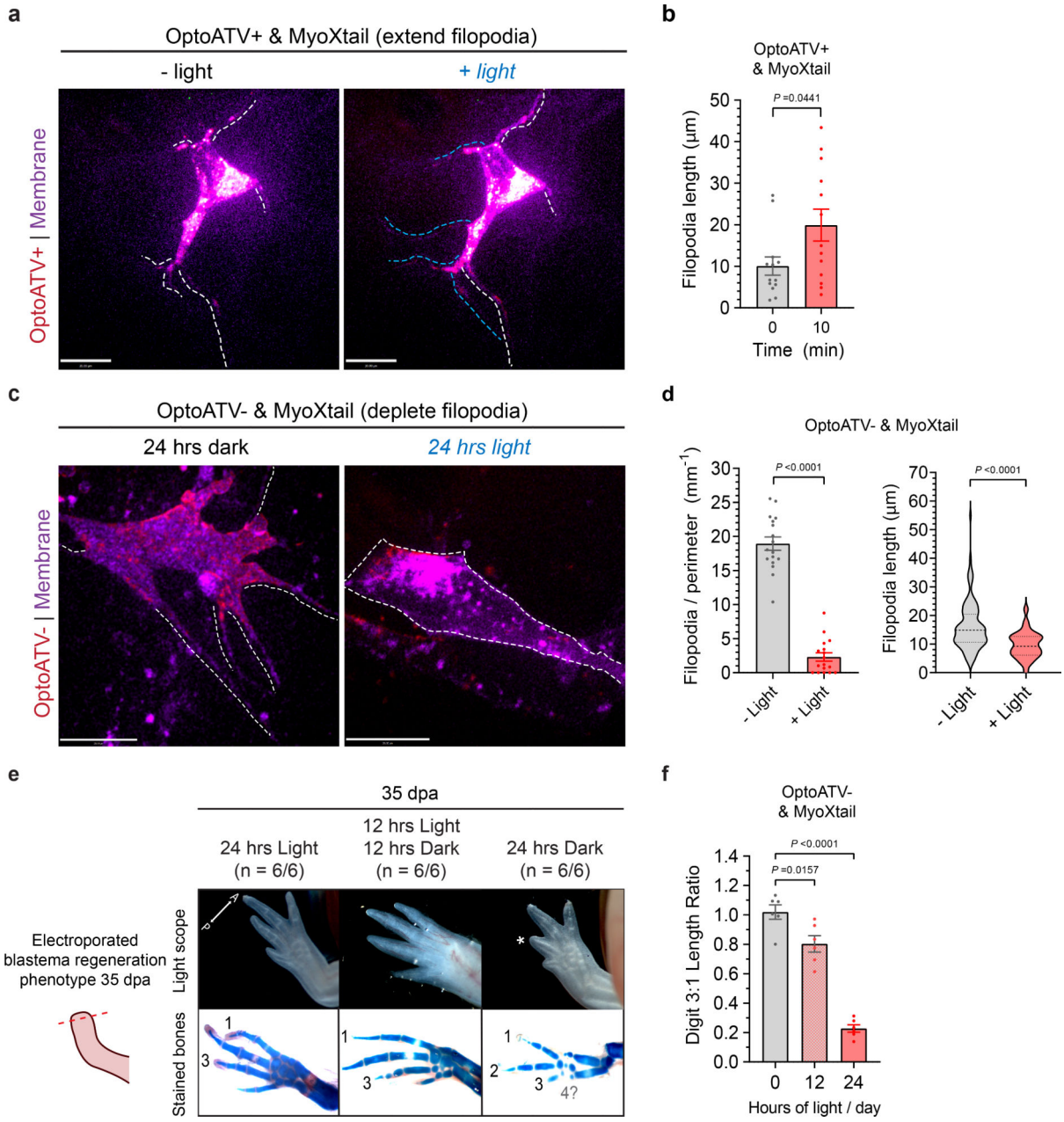

Figure 6. Applications of optoATVs to manipulate filopodia dynamics in the axolotl blastema cause selective regeneration defects

(a, b) Expression of mKate2-optoATV+ and eGFP-MyoXtail in axolotl blastema shows elongation of filopodia upon 5 short pulses of blue light stimulation. (a) Representative images chosen from 3 independent experiments. White dashed lines delineate the filopodia, while blue dashed lines highlight the elongated filopodia. Scale, 20 μm. (b) Quantification of the filopodia length after light activation (N = 13 filopodia from 3 animals). Statistics determined by two-tailed Mann Whitney test.

(c, d) Expression of mKate2-optoATV− and eGFP-MyoXtail in axolotl blastema under consistent ambient light shows reduction of filopodia for each cell. (c) Representative images chosen from 4 independent experiments. White dashed lines delineate the filopodia

(left) or the cell border (right). Scale, 20 μm. (d) Quantification of filopodia density of each individual cell (left, N = 17 cells each) and filopodia length (right, N = 118 and 30 filopodia each). The violin plot displays the median and quartiles using dotted lines. Statistics determined by two-tailed Mann-Whitney test.
(e, f) Effects of filopodia reduction on limb regeneration at 35 dpa. (e) Upper lane shows the light microscope images, and the lower lane shows the bone staining images. The asterisks indicate the affected posterior digits, and the numbers indicate the digit numbers. Representative images chosen from 6 independent experiments. A, anterior; P, posterior. (f) Quantification of the length ratio of digit 3 against digit 1 (N = 6 animals each). Statistics determined by two-tailed Welch's ANOVA test and Dunn's post-hoc test.
All bar graphs displayed as mean ± SEM.

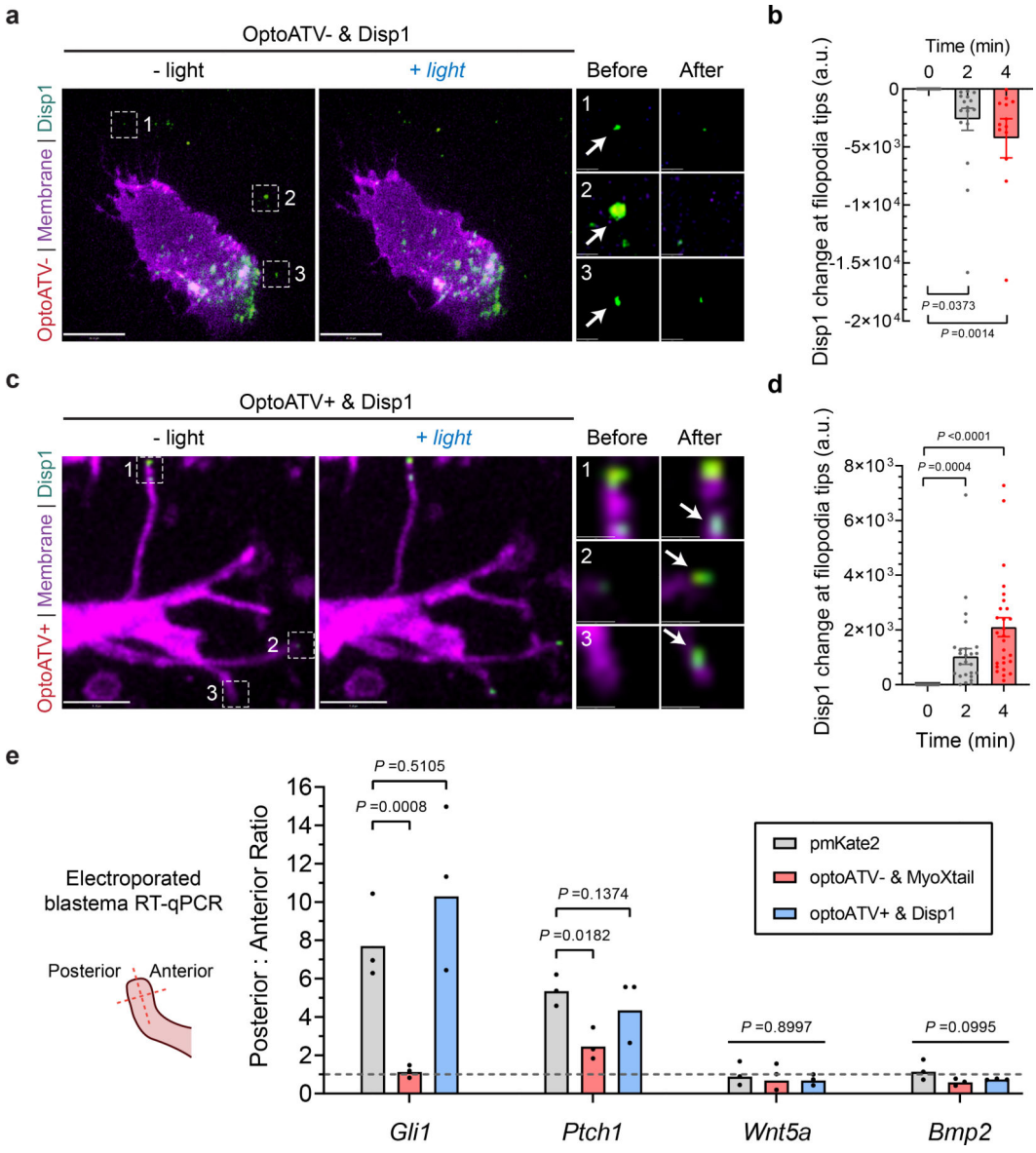

Figure 7. Applications of optoATVs in the axolotl blastema reveal the critical role of filopodia in re-establishing Shh gradient during tissue regeneration

(a, b) Expression of mKate2-optoATV+ and Disp1-eGFP in axolotl blastema shows rapid transport of Disp1-eGFP towards filopodia tips upon light stimulation. (a) Representative images chosen from 3 independent experiments. Accumulation of Disp-eGFP at tips are indicated by white arrows. Scale, 20 μm (original) or 5 μm (magnified). (b) Quantification of Disp1-eGFP concentration change at filopodia tips after light activation (N = 27 filopodia). Statistics determined by two-tailed Friedman test and Dunn's post-hoc test. The bar graph displayed as mean ± SEM.

(c, d) Expression of mKate2-optoATV− and Disp1-eGFP in axolotl blastema shows depletion of Disp1-eGFP from filopodia upon light stimulation. (c) Representative images chosen from 3 independent experiments. Numbered white dashed boxes indicating the depletion of Disp1-eGFP at filopodia tips (pointed by white arrows) are magnified on the

right. Scale, 20 μm (original) or 1 μm (magnified). (d) Quantification of Disp1-eGFP depletion at tips after light activation (N = 18 filopodia). Statistics determined by two-tailed Friedman test and Dunn's post-hoc test. The bar graph displayed as mean ± SEM.
(e) Signaling gradients of the Shh, Wnt and Bmp pathways as quantified by the relative gene expression ratio of the posterior against anterior sections (N = 3 animals each). A simplified scheme of the microdissection is shown on the left. (Right) The gray dashed line represents an equal ratio. Statistics determined by two-tailed Welch's ANOVA test and Dunn's post-hoc test based on log-transformed relative gene expression values. The bar graph displays the geometric mean.